"HIFU Beam:" A Simulator for Predicting Axially Symmetric Nonlinear Acoustic Fields Generated by Focused Transducers in a Layered Medium

Petr V. Yuldashev, Maria M. Karzova, Wayne Kreider, Pavel B. Rosnitskiy, Oleg A. Sapozhnikov, and Vera A. Khokhlova

***Abstract*— "HIFU beam" is a freely available software tool that comprises a MATLAB toolbox combined with a user-friendly interface and binary executable compiled from FORTRAN source code (*HIFU beam*. (2021). Available: http://limu.msu.ru/node/3555?language =en). It is designed for simulating high-intensity focused ultrasound (HIFU) fields generated by single-element transducers and annular arrays with propagation in flat-layered media that mimic biological tissues. Numerical models incorporated in the simulator include evolution-type equations, either the Khokhlov–Zabolotskaya–Kuznetsov (KZK) equation or one-way Westervelt equation, for radially symmetric ultrasound beams in homogeneous and layered media with thermoviscous or power-law acoustic absorption. The software uses shock-capturing methods that allow for simulating strongly nonlinear acoustic fields with high-amplitude shocks. In this article, a general description of the software is given along with three representative simulation cases of ultrasound transducers and focusing conditions typical for therapeutic applications. The examples illustrate major nonlinear wave effects in HIFU fields including shock formation. Two examples simulate propagation in water, involving a single-element source (1-MHz frequency, 100-mm diameter, 90-mm radius of curvature) and a 16-element annular array (3-MHz frequency, 48-mm diameter, and 35-mm radius of curvature). The third example mimics the scenario of a HIFU treatment in a "water-muscle-kidney" layered medium using a source typical for abdominal HIFU applications (1.2-MHz frequency, 120-mm diameter, and radius of curvature). Linear, quasi-linear, and shock-wave exposure protocols are considered. It is intended that "HIFU beam" can be useful in teaching nonlinear acoustics; designing and characterizing high-power transducers; and developing exposure protocols for a wide range of therapeutic applications such as shock-based HIFU, boiling histotripsy, drug delivery, immunotherapy, and others.**

***Index Terms*— Biological tissue, developed shock, equivalent source, "HIFU beam" software, Khokhlov–Zabolotskaya–Kuznetsov (KZK) equation, shock wave, Westervelt equation, wide-angle parabolic approximation.**

I. Introduction

NUMERICAL modeling of ultrasound fields is an effective tool in modern high-intensity focused ultrasound (HIFU) research and applications. The current paper describes a software that has been created to contribute to this approach [1]. Simulations are used for the design and characterization of HIFU transducers of different types and geometries [2]–[7] and also for quantitative estimation of ultrasound field parameters such as peak pressures, intensity, and heating rate in phantoms and biological tissues [8]–[11]. Modeling plays a critical role in developing, testing, and evaluating the efficiency and safety of HIFU protocols. The overall utility and importance of numerical modeling have significantly grown over the last two decades due to a tremendous increase in computer processing power, parallel computations, and development of new numerical algorithms [12]. These advancements have made it possible to consider more realistic problems including ultrasound propagation in inhomogeneous biological tissues [13]–[16].

Progress in modeling and simulation tools is also reflected in international standards related to medical ultrasound. In 2014, a Technical Specification was released by the International Electrotechnical Commission (IEC) for characterizing therapeutic ultrasound fields with the inclusion of options for numerical calculation of some field parameters [17]. Related work within IEC Technical Committee 87 continues toward the standardization of methods for measurement-based modeling. Moreover, computational studies are recognized by a formal guidance document as a potential part of medical device submissions to the U.S. Food and Drug Administration [18].

Various wave propagation models based on different wave equations and numerical algorithms have been developed [19], [20]. An effective strategy is to publish numerical

Manuscript received January 10, 2021; accepted April 15, 2021. Date of publication April 20, 2021; date of current version August 27, 2021. The work was supported in part by the Russian Science Foundation under Grant 20-12-00145 and in part by the National Institutes of Health under Grant R01EB7643 and Grant R01EB025187. *(Corresponding author: Petr V. Yuldashev.)*

Petr V. Yuldashev, Maria M. Karzova, and Pavel B. Rosnitskiy are with the Faculty of Physics, M. V. Lomonosov Moscow State University, 119991 Moscow, Russia (e-mail: petr@acs366.phys.msu.ru).

Wayne Kreider is with the Center for Industrial and Medical Ultrasound, Applied Physics Laboratory, University of Washington, Seattle, WA 98105 USA.

Oleg A. Sapozhnikov and Vera A. Khokhlova are with the Faculty of Physics, M. V. Lomonosov Moscow State University, Moscow 119991, Russia, and also with the Center for Industrial and Medical Ultrasound, Applied Physics Laboratory, University of Washington, Seattle, WA 98105 USA.

Digital Object Identifier 10.1109/TUFFC.2021.3074611

models and to develop and distribute software where a particular equation and corresponding numerical method are implemented. These software packages can then be used to solve typical ultrasound wave propagation problems [21]–[28].

In this introduction, we primarily focus on references that correspond to the specific features of such freely available ultrasound simulation software. For a broader overview, we refer to other papers that present different ultrasound modeling methods relevant to the "HIFU beam" software [29]–[33].

In general, ultrasound simulation models can be divided into three broad categories. In the first category, a 3-D full-wave equation is solved. This solution allows for wave propagation in inhomogeneous media including important phenomena such as nonlinear effects, multiple-scattering, and reflection [12], [34]–[36]. A commonly used example is the freely available "*k*-Wave" software which solves a full-wave equation in *k*-space using a pseudospectral method [26]. The "*k*-Wave" software can be used to simulate both linear and nonlinear propagation in inhomogeneous biological tissues with features such as frequency-dependent power-law absorption and corresponding dispersion. Another software version was developed for acoustic wave propagation in an elastic medium and was used to simulate ultrasound propagation through the skull [14], [37]. However, in its 3-D formulation, "*k*-Wave" is very demanding in terms of computer processing power and memory, especially for ultrasound fields involving nonlinear propagation and the presence of more than a few harmonics [11]. Even for weakly nonlinear fields, it is recommended that simulations be performed on high-end desktop computers, workstations, or clusters [38].

In the second category, simplified wave equations are solved assuming one-way propagation. For simulating 3-D ultrasound beams, either the KZK equation [39], [40] or the Westervelt equation [41]–[44] is used. The angular spectrum method is frequently implemented for calculating the diffraction operator in the one-way form of the Westervelt equation [32], [45]. Several publicly available software packages leverage this approach. The "Abersim" solver can simulate 3-D propagation of wide-band slightly nonlinear acoustic pulses from arbitrarily shaped transducers [24], [46]. The ultrasound simulator "FOCUS," developed at Michigan State University, uses the fast nearfield method to initialize pressure fields generated by transducers with prescribed geometries [23]. The initial pressure field is then propagated linearly using the angular spectrum method [47]. Additionally, "FOCUS" includes routines for steady-state and transient wavefield simulations with the KZK equation [48]. The software "CREANUIS" realized the generalized angular spectrum method that allows for simulation of the fundamental and second-harmonic pressure fields in the quasi-linear approximation by accounting for homogeneous or inhomogeneous nonlinear properties of the propagation medium [27]. "CREANUIS" is primarily used to simulate diagnostic ultrasound fields and to test different harmonic imaging techniques [49]. While the efficiency of such 3-D one-way algorithms is much higher than full-wave modeling, only moderately nonlinear problems have been modeled using standard personal computers. However, simulation of 3-D shock-wave fields from arbitrary-shaped transducers in the one-way approach can be performed using supercomputers [5], [44].

The third category is based on one-way propagation equations such as the Khokhlov–Zabolotskaya–Kuznetsov (KZK) equation limited to consideration of axially symmetric beams [21], [22], [25], [50], [51]. Such solvers are significantly more efficient compared to the 3-D wave models and can therefore be used to simulate strongly nonlinear fields with shocks on standard personal computers. For example, a frequency-domain KZK solver for axially symmetric beams known as the "Bergen" code was developed in the early 1990s [21]. Another software package based on the KZK equation for simulating axially symmetric high-intensity focused ultrasound beams included a solver of the Pennes bioheat transfer equation and was packaged for MATLAB (The Mathworks, Inc., Natick, MA, USA) [25]. This software has been subsequently enhanced by replacing the diffraction operator in the parabolic approximation by the diffraction operator using a wide-angle parabolic approximation (WAKZK) and now is known as "HITU_Simulator" [51]. The KZK version of the software was also extended to account for acoustic beam propagation through multiple flat layers of different biological tissues [52]. In all versions, the nonlinear term was solved in the frequency domain by numerically integrating a coupled system of nonlinear equations for harmonic amplitudes. This process requires high computational resources for modeling high-amplitude shocks because the number of operations is proportional to the square of the number of harmonics included in simulations. Soon after the Bergen code, a KZK time-domain solver for axially symmetric beams was developed and published in the form of a FORTRAN source code known as the Texas Code or KZKTEXAS [22]. This code has been used for modeling pulses with shocks but suffers from strong artificial absorption due to the interpolation procedure in modeling the nonlinear term.

The goal of this article is to present a new "HIFU beam" solver designed for simulating nonlinear acoustic fields generated by single-element HIFU transducers and annular arrays in flat-layered media that mimic biological tissue [1]. The software was developed for use on standard personal computers as a MATLAB application combined with a binary executable compiled from FORTRAN source code. The major distinguishing features of "HIFU beam" are the ability for efficient simulation of high-amplitude shocks using a shock-capturing scheme, propagation in flat-layered media, implementation of a realistic boundary condition for focused ultrasound transducers, and a user-friendly interface. The development of "HIFU beam" and its experimental validation reflects the experience of more than 20 years of collaborative research on therapeutic ultrasound-based applications between the Laboratory of Industrial and Medical Ultrasound (LIMU) at M. V. Lomonosov Moscow State University (Moscow, Russia) and the Center for Industrial and Medical Ultrasound (CIMU) at the University of Washington (Seattle, WA, USA) [5], [44], [53]–[62].

The numerical models incorporated in the simulator are based on evolution-type equations, either KZK or one-way Westervelt-type equations, for radially symmetric ultrasound beams in homogeneous and layered media with thermoviscous

or power-law frequency dependence of acoustic absorption and corresponding dispersion. The differences between the two models available in the simulator are the approximations used to solve the diffraction operator and to set the boundary conditions to the model. When solving the KZK equation, the diffraction for each harmonic component of the wave is accounted for in the parabolic approximation (KZK-mode), whereas the diffraction term in the Westervelt equation is solved using a wide-angle Padé approximation (WAPE-mode) [33], [62]. An equivalent source model is included in the software for the KZK solver for a more accurate simulation of strongly focused beams [59]. The core functionality of the application of both KZK and WAPE modes is provided by finite-difference numerical schemes. The nonlinear operator is solved in the frequency domain for slightly distorted waveforms and in the time domain using a shock-capturing scheme for strongly distorted waveforms. The absorption and dispersion operator is solved in the frequency domain using an exact solution for each harmonic component.

A graphical user interface (GUI) to the software has been designed for flexibility and user-friendliness. The interface uses MATLAB GUI functionality to set user-defined input parameters to the numerical model, to run simulations, and to read and visualize the output data. "HIFU beam" optionally uses a text interface based on MATLAB scripts and functions, which is not described in the current paper. The computational engine is compiled to a binary file from FORTRAN 2003 source code and is compliant with Windows operating systems (Microsoft Inc., Redmond, WA, USA). The binary code has been optimized for speed, accuracy, and parallel execution on multicore processors. This software is still under development and its functionality is still evolving. We hope that user feedback can help us to make it better.

II. Numerical Model

In this section, we describe for "HIFU beam" the governing equations, the numerical algorithms used to solve these equations, the methods used to set model boundary conditions, and the options for defining multilayer propagation media. Two simulation modes available in Version 1.0, KZK and WAPE, are based, respectively, on the KZK parabolic equation and the one-way Westervelt-type equation in a wide-angle parabolic approximation of the diffraction effects.

A. Radially Symmetric KZK Equation (KZK-Mode)

The KZK-mode utilizes a solver of the KZK equation, which models nonlinear propagation of acoustic beams in a thermoviscous medium and accounts for diffraction effects in the parabolic approximation. Here, the KZK equation is considered for radially symmetric acoustic beams and generalized to account for frequency-dependent absorption in a homogeneous tissue-like medium

$$\frac{\partial^2 p}{\partial \tau \partial z} = \frac{c_0}{2}\left(\frac{\partial^2 p}{\partial r^2} + \frac{1}{r}\frac{\partial p}{\partial r}\right) + \frac{\beta}{2\rho_0 c_0^3}\frac{\partial^2 p^2}{\partial \tau^2} + \frac{\delta}{2c_0^3}\frac{\partial^3 p}{\partial \tau^3} + L_a(p). \quad (1)$$

Here, p is the acoustic pressure, z is the spatial coordinate along the beam axis, r is the radial coordinate, and $\tau = t - z/c_0$ is the retarded time. Parameters ρ_0, c_0, β, and δ are the ambient density, isentropic sound speed, nonlinearity coefficient, and diffusivity of sound in the propagation medium, respectively. The three differential operators from left to right on the right-hand side of (1) correspond to diffraction, nonlinear, and thermoviscous absorption effects. The last operator generally has an integral form and corresponds to frequency-dependent absorption and dispersion effects in biological tissue and is discussed separately.

B. Radially Symmetric Westervelt Equation (WAPE-Mode)

The WAPE-mode of the software corresponds to solving the one-way Westervelt equation with radial symmetry. The equation can be written in the retarded time coordinate system as follows:

$$\frac{\partial^2 p}{\partial \tau \partial z} = \frac{c_0}{2}\left(\frac{\partial^2 p}{\partial z^2} + \frac{\partial^2 p}{\partial r^2} + \frac{1}{r}\frac{\partial p}{\partial r}\right) + \frac{\beta}{2\rho_0 c_0^3}\frac{\partial^2 p^2}{\partial \tau^2} + \frac{\delta}{2c_0^3}\frac{\partial^3 p}{\partial \tau^3} + L_a(p). \quad (2)$$

The only difference between the KZK and Westervelt equations in (1) and (2) is in the diffraction operator represented by the first term on the right-hand side. The diffraction operator of the Westervelt equation contains an extra second-order derivative of the pressure over the axial coordinate z. This difference reflects the fact that the diffraction operator of the Westervelt equation exactly corresponds to the linear wave equation, while the KZK uses a small diffraction angle approximation. This difference results in different accuracies for simulating focused beams, with the Westervelt equation being more accurate in the presence of high focusing angles. However, it is possible to achieve good accuracy with the KZK model even for highly focused beams by modifying the source boundary conditions as described in Sections II-F and IV-A.

C. Power Law Absorption in Biological Tissue

The last linear operator $L_a(p)$ in both (1) and (2) accounts for a power law of absorption as a function of frequency along with corresponding dispersion as typical for biological tissues [63]. In the frequency domain, the absorption coefficient at an arbitrary angular frequency ω is represented as

$$\alpha(\omega) = \alpha_0\left(\frac{\omega}{\omega_0}\right)^{\eta}. \quad (3)$$

Here, α_0 is the absorption coefficient at the angular frequency of the source ω_0, and the exponent parameter η is typically close to unity for biological tissues [63]. Dispersion $c(\omega)$ is introduced according to the approximate local Kramers–Kronig dispersion relations, which in the case of weak dispersion and $0 < \eta < 2$ can be written as

follows:

$$\frac{\Delta c}{c_0} = \frac{c(\omega) - c_0}{c_0} = \begin{cases} -\dfrac{c_0\alpha_0}{\omega_0}\tan\left(\dfrac{\pi}{2}\eta\right)\left[\left(\dfrac{\omega}{\omega_0}\right)^{\eta-1} - 1\right], & \eta \neq 1 \\ \dfrac{2c_0\alpha_0}{\pi\omega_0}\ln\left(\dfrac{\omega}{\omega_0}\right), & \eta = 1. \end{cases} \tag{4}$$

where $c_0 = c(\omega_0)$ [64]. Note, that in tissue-mimicking layers the thermoviscous absorption term is included along with power-law absorption, since a quadratic dependence of the absorption coefficient on frequency is needed to keep a finite rise time of the shock front [53]. For weakly nonlinear cases, thermoviscous absorption calculated for parameters of water is very weak and is overwhelmed by power-law absorption in tissue.

D. Numerical Algorithms

Numerical solutions to the KZK and Westervelt equations are based on the fractional steps method with an operator-splitting procedure of second-order accuracy [32], [44], [46]. According to this method, different physical effects represented by separate operators on the right-hand side of (1) and (2) are calculated one after another in the frequency-domain or time-domain at each propagation step Δz along the axial coordinate. At each spatial point (r, z) of the numerical grid, the pressure field is stored as a set of complex harmonic amplitudes p_n of a Fourier series expansion

$$p(\tau, r, z) = \sum_{n=-N_{\max}}^{N_{\max}} p_n(r, z)\exp(-in\omega_0\tau). \tag{5}$$

Here, i is the imaginary unit and $\omega_n = n\omega_0$ is the angular frequency of the nth harmonic. The maximal number of harmonics, $N_{\max}$, is defined by the user and is typically equal to $N_{\max} = 1000$. Frequency domain storage of the pressure field is preferable since all operators are solved in the frequency domain, with the exception of the nonlinear operator when shocks are present.

The diffraction operator in both (1) and (2) is solved in the frequency domain, separately for each Fourier harmonic p_n with the corresponding wavenumber $k_n = n\omega_0/c_0$.

The parabolic diffraction equation related to the KZK equation is [50]

$$\frac{\partial p_n}{\partial z} = \frac{i}{2k_n}\Delta_\perp p_n = \frac{i}{2k_n}\frac{1}{r}\frac{\partial}{\partial r}\left(r\frac{\partial p_n}{\partial r}\right). \tag{6}$$

This equation is discretized in the radial direction using the second-order finite differences on a uniform grid [22], [62]. Close to the source, a fully implicit algorithm of the first-order accuracy and strong absorption is used to damp oscillations produced by sharp edges of the source boundary condition [22]. At longer distances, the solver switches to the less absorptive Crank–Nicolson scheme with second-order accuracy in both z and r coordinates. The resulting tridiagonal systems of linear equations for discretized pressure amplitudes are solved by the Thomas algorithm [65].

The diffraction operator of the Westervelt equation in the frequency domain reduces to the Helmholtz equation for each Fourier harmonic p_n. Considering a unidirectional assumption about the propagating beam, the Helmholtz equation is replaced by a one-way pseudodifferential equation [66]

$$\frac{\partial p_n}{\partial z} = ik_n\left(\sqrt{1 + \frac{\Delta_\perp}{k_n^2}} - 1\right)p_n \tag{7}$$

which is solved using methods developed in the theory of wide-angle parabolic equations [67]. In particular, a split-step Padé approximation method is used which includes several specific steps [68]. First, a formal solution of (7) with an exponential operator is written as

$$p_n(r, z + \Delta z) = \exp\left[ik_n\Delta z\left(\sqrt{1 + \frac{\Delta_\perp}{k_n^2}} - 1\right)\right]p_n(r, z). \tag{8}$$

Second, the exponential operator in (8) is approximated using a Padé approximation of order (M, M)

$$\exp\left[ik_n\Delta z\left(\sqrt{1 + \frac{\Delta_\perp}{k_n^2}} - 1\right)\right] \approx \prod_{m=1}^{M}\frac{1 + \mu_m(ik_n\Delta z)\Delta_\perp/k_n^2}{1 + \nu_m(ik_n\Delta z)\Delta_\perp/k_n^2}. \tag{9}$$

Increasing the approximation order M reduces the difference between the exact exponential operator and its Padé approximation. The software default is $M = 3$ and can be altered in the text-based interface.

As a result, the pressure field of the nth harmonic at the next step of the algorithm is obtained by sequentially solving M intermediate equations

$$\left(1 + \mu_m(ik_n\Delta z)\frac{\Delta_\perp}{k_n^2}\right)\tilde{p}_n^{m+1} = \left(1 + \nu_m(ik_n\Delta z)\frac{\Delta_\perp}{k_n^2}\right)\tilde{p}_n^m \tag{10}$$

where $\tilde{p}_n^0 = p_n(r, z)$, $\tilde{p}_n^M = p_n(r, z + \Delta z)$, $m = 0 \ldots M - 1$. Split-step Padé approximation coefficients $\mu_m(ik_n\Delta z)$ and $\nu_m(ik_n\Delta z)$ are evaluated as described in the literature without damped evanescent waves [29].

Equation (10) is discretized using a finite-difference scheme similar to the Crank–Nicolson scheme of the classic parabolic (6). The resulting tridiagonal systems of linear equations are solved using the Intel MKL (Math Kernel Library) routines for tridiagonal systems with partial pivoting because the systems are not diagonally dominant. The algorithm execution for different harmonics is organized in parallel. A detailed description of the split-step wide-angle diffraction algorithm implemented in the solver is given in [62].

To prevent artificial reflections from the outer radial boundary of the computational domain, a perfectly matching layer (PML) is included in both the classical parabolic equation and the wide-angle equation [30]. The PML attenuation coefficient $\sigma(r)$ is gradually increased from the initial PML radial coordinate r_{PML} to the outer boundary R_{Len} according to cubic parabola law

$$\sigma(r) = \sigma_0\left(\frac{r - r_{\text{PML}}}{R_{\text{Len}} - r_{\text{PML}}}\right)^3. \tag{11}$$

By default, the width of the PML $R_{\text{Len}} - r_{\text{PML}}$ is set to be equal to 10 mm and the ratio σ_0/ω_0 is set to 10. These default parameters of the PML were used to produce simulation results presented below in Section IV.

The nonlinear and absorption operators have the same forms in both KZK and Westervelt equations; consequently, identical methods are used to calculate them. The nonlinear operator is represented in a form of the simple wave equation

$$\frac{\partial^2 p}{\partial \tau \partial z} = \frac{\beta}{2\rho_0 c_0^3} \frac{\partial^2 p^2}{\partial \tau^2}. \tag{12}$$

At small distances z close to the source, where the acoustic wave is not strongly distorted due to nonlinear propagation effects, the nonlinear operator is solved in the frequency domain by integrating a system of coupled nonlinear equations for harmonic amplitudes using a fourth-order Runge–Kutta method [50], [53]

$$\frac{\partial p_n}{\partial z} = -\frac{in\beta}{\rho_0 c_0^3}\left(\sum_{k=1}^{N-n} p_k^* p_{n+k} + \frac{1}{2}\sum_{k=1}^{n-1} p_k p_{n-k}\right). \tag{13}$$

The number of harmonics N at the current spatial location is varied adaptively by comparing the amplitude of the last Nth harmonic included in simulations with a specified threshold. As a result, the number of harmonics is increased with increasing waveform distortion and decreased otherwise. An adaptive approach is also applied to the outer boundary R_{Len} in the diffraction algorithms calculated individually for each harmonic based on a specified threshold. This optimization greatly saves computation time for slightly distorted waveforms by avoiding a Fourier transform of the solution from the frequency domain to the time domain and back.

Before the formation of shock fronts in the pressure waveform in a given spatial location, the nonlinear solver is automatically switched to the time-domain conservative Godunov-type shock-capturing scheme [31]. This transition is programmed to occur when the amplitude of the tenth harmonic exceeds 1% of the amplitude of the fundamental frequency [44]. An inverse Fourier transform implemented in Intel MKL is then used to construct time-domain waveform from pressure harmonics stored in computer memory. Nonlinear algorithms are executed in parallel for different spatial points along the radial axis.

The absorption term is calculated in the frequency domain based on the exact analytic solution for each of the harmonics. The term includes both thermoviscous absorption and power-law absorption, as well as dispersion:

$$p_n(z+\Delta z) = p_n(z)\exp\left[\frac{i\omega_n \Delta c(\omega_n)}{c_0^2}\Delta z - \left(\frac{\delta\omega_n^2}{2c_0^3} + \alpha(\omega_n)\right)\Delta z\right] \tag{14}$$

where $\Delta c(\omega_n) = c(\omega_n) - c(\omega_0)$. Absorption and dispersion exponents for each harmonic frequency and material layer at the current propagation distance are precalculated, stored in memory, and used to multiply spectral components of the pressure field at each propagation substep of the absorption operator. In order to keep a given value of the rise time of the shock front, the thermoviscous diffusivity δ is artificially increased depending on the shock front amplitude at a local spatial point [61]. Artificial absorption allows for a significant decrease of oscillations which appear when shock fronts are formed and large pressure field gradients develop across the radial direction. This increase in absorption does not affect the waveform except for the steepness of the shock front [61].

E. Layered Medium

"HIFU beam" allows for simulation of propagation through biological tissue layers by using a flat-layered medium model. In the current version of the software, when the solution reaches a plane boundary between two layers, pressure harmonic amplitudes are multiplied by the classical pressure transmission coefficient for a normally incident wave

$$\frac{p_{n,2}}{p_{n,1}} = \frac{2\rho_2 c_2}{\rho_2 c_2 + \rho_1 c_1}. \tag{15}$$

Here $p_{n,2}$, c_2, ρ_2 and $p_{n,1}$, c_1, ρ_1 are harmonic amplitudes, sound speed, and density in the next and current layers, respectively. In the next layer, the harmonic wavenumbers are updated and the marching algorithm continues with new medium parameters. Reflected waves are neglected due to the one-way nature of the model.

F. Source Boundary Conditions

The source boundary conditions for the KZK and Westervelt equations are set in separate ways. By default, only a focused source can be simulated using the GUI. In KZK-mode, a uniform pressure amplitude distribution p_1 is set at the plane $z = 0$ for a piston source of diameter D with an optional central opening of diameter d, focal distance F, and operational angular frequency ω_0. A complex pressure amplitude corresponding to the real pressure magnitude p_0 is set by an analytical expression which includes parabolic focusing of phase [2]

$$p_1 = \begin{cases} \dfrac{p_0}{2}\exp\left(-i\dfrac{k_0 r^2}{2F}\right), & \dfrac{d}{2} \le r \le \dfrac{D}{2} \\ 0, & r < \dfrac{d}{2}, \quad r > \dfrac{D}{2}. \end{cases} \tag{16}$$

This parabolic form of the boundary condition can adequately describe the acoustic field only for weakly focused transducers with high F-numbers ($F/D > 1.9$), defined as a ratio of the focal distance to the diameter [69], [70]. In order to extend the applicability of the KZK equation for simulating strongly focused transducers, a method of an equivalent source has been proposed and demonstrated for the case of a single-element spherical bowl transducer without a central opening ($d = 0$) [59], [60], [62]. The idea of the equivalent source method is to match the location of the prefocal and postfocal nulls and the amplitude of the focal lobe, considering the fields generated by both a spherically focused transducer obtained in linear approximation using the Rayleigh integral [71] and the solution of a linear parabolic equation. As a result, analytical formulae have been derived to describe the diameter D_{eq}, focal distance F_{eq}, and pressure

amplitude $p_{0\text{eq}}$ of an equivalent source from the corresponding parameters D, F, and p_0 of a spherical bowl source [59]

$$\begin{cases} \dfrac{F_{\text{eq}}}{D_{\text{eq}}} = \dfrac{1}{2\sqrt{2\pi}}\left(\dfrac{\sigma_1\sigma_2}{\sigma_1-\sigma_2}\right)^{1/2}, \\ k_0 F_{\text{eq}} = -\dfrac{2\sigma_1\sigma_2}{\sigma_1+\sigma_2}, \\ \dfrac{p_{0\text{eq}}}{p_0} = 4\left(\dfrac{F_{eq}}{D_{eq}}\right)^2 \dfrac{F}{F_{eq}}\left(2-\sqrt{4-\left(\dfrac{D}{F}\right)^2}\right) \end{cases} \tag{17}$$

where

$$\sigma_{1,2} = 4\pi\left(\frac{F}{D}\right)\frac{k_0F(\mp k_0F-\pi)\cdot\sqrt{4(F/D)^2-1}\mp 2(F/D)\left[(k_0F)^2\pm 3\pi k_0F+2\pi^2\right]}{(k_0F)^2+16\pi(\pi\pm k_0F)(F/D)^2}.$$

Equivalent source parameters are then substituted into (16) to set an initial pressure field for a single-element focused transducer. Comparison of nonlinear fields simulated using the KZK equation with an equivalent source model and the Westervelt equation with more realistic boundary conditions described below show that very good accuracy is achieved for nonlinear wave parameters around the focal maximum of the beam [60], [62]. A typical difference is shown below in Fig. 7 and is less than 3% excluding tiny details related to shock-shock interaction described in Section IV-A.

The source boundary condition to the Westervelt equation is set by calculating a pressure hologram using the Rayleigh integral [72]. A source is assumed to have a shape of a spherical bowl with a given radius of curvature, external diameter, optional central opening, and uniform distribution of the vibration velocity u_n on its surface. For generality, an annular array pattern with an arbitrary number of elements of equal surface can be defined on the spherical surface, with a distinct velocity magnitude and phase assigned to each element. Spacing gaps between the array elements also can be specified by the user. The characteristic pressure amplitude p_0 on the surface of each array element is calculated by assuming the plane wave relation $p_0 = |u_n|\rho_0 c_0$.

In order to calculate the Rayleigh integral, the active surface of the array is covered by a mesh of triangles with side lengths several times smaller than the wavelength at the fundamental frequency. The normal component of the velocity u_n is specified at the surface of each triangle. For electronic focus steering along the axial direction z, a phase for each element is calculated from the path length difference between the central rim of the circular element and the position of the steered focus. The radius of the central rim is calculated from the mean value of polar angles of the internal and external rims of the element. The calculated phase is included in the complex amplitude of the oscillation velocity of all triangles belonging to a given element of the array. Then, the pressure amplitude distribution along the radial coordinate is calculated at the axial distance halfway between the source and the geometrical focus. Finally, the hologram is propagated backward to the initial plane, $z = 0$, using the same wide-angle diffraction algorithm described in the previous sections. The resulting pressure field is tapered by a smooth spatial filter to achieve zero pressure amplitude inside the PML layer and is used as a boundary condition.

G. Output Data

While simulations are performed over the coordinate z, acoustic field data are collected and stored for user-specified spatial locations in the (r, z) plane. Data include pressure magnitudes of the first several harmonics, pressure waveforms, peak positive, and peak negative pressures in the acoustic waveform, intensity, and heat sources. In KZK-mode, the intensity is calculated in a plane wave approximation as [25], [53]

$$I_p = \frac{2}{\rho_0 c_0}\sum_{n=1}^{N_{\max}} |p_n|^2. \tag{18}$$

In the WAPE-mode, the z-component of intensity is calculated as

$$I_w = \frac{2}{\rho_0 c_0}\sum_{n=1}^{N} Re\left(p_n^*\sqrt{1+\frac{\Delta_\perp}{k_n^2}}\,p_n\right) \tag{19}$$

for the first 20 harmonics; however, for higher harmonics the plane wave approximation from (18) is used to save computational time. Equation (19) is the sum of products of harmonics of the complex conjugate of acoustic pressure and the z-component of the acoustic velocity vector in which the pseudodifferential operator is calculated using the Padé approximations of the square-root operator [66], [73]. In the current version of the "HIFU beam" software, heat sources are calculated in a quasi-plane wave approximation as a difference of intensities using (18) on the previous and on the next z distances when applying nonlinear and absorption operators divided by the marching step Δz [58].

III. HIFU Beam GUI Main Screen Structure

The main screen of the "HIFU beam" software is shown in Fig. 1. A logo, which normally appears separately when starting the program, is attached to the right. The main screen is partitioned into several areas, which control different groups of user-defined input parameters. In the central area of the screen, the geometry of the problem is depicted, including a contour of a spherical bowl source, the position of the focus, layers of the propagation medium, and a rectangular box containing the output domain. At the bottom, parameters describing the propagation medium layers are grouped. Here the user can define the number of layers, axial positions of their boundaries, acoustic properties of each layer, display colors, and labels. Custom lists of materials and their acoustic parameters can be created, stored for future use, and loaded. In the upper left part of the screen, two push buttons are located: "Run" and "Results." The "Run" button launches simulations and the "Results" button pulls up an additional window for displaying data.

Below these buttons on the left of the main screen, source parameters are grouped. The main geometrical parameters of an annular array are specified together with source pressure amplitude p_0, corresponding intensity $I_0 = p_0^2/2\rho_0 c_0$, and total acoustic power of the source W_0 calculated as a product of active radiating surface of the source and intensity I_0. The number of elements is set to one if a single-element transducer

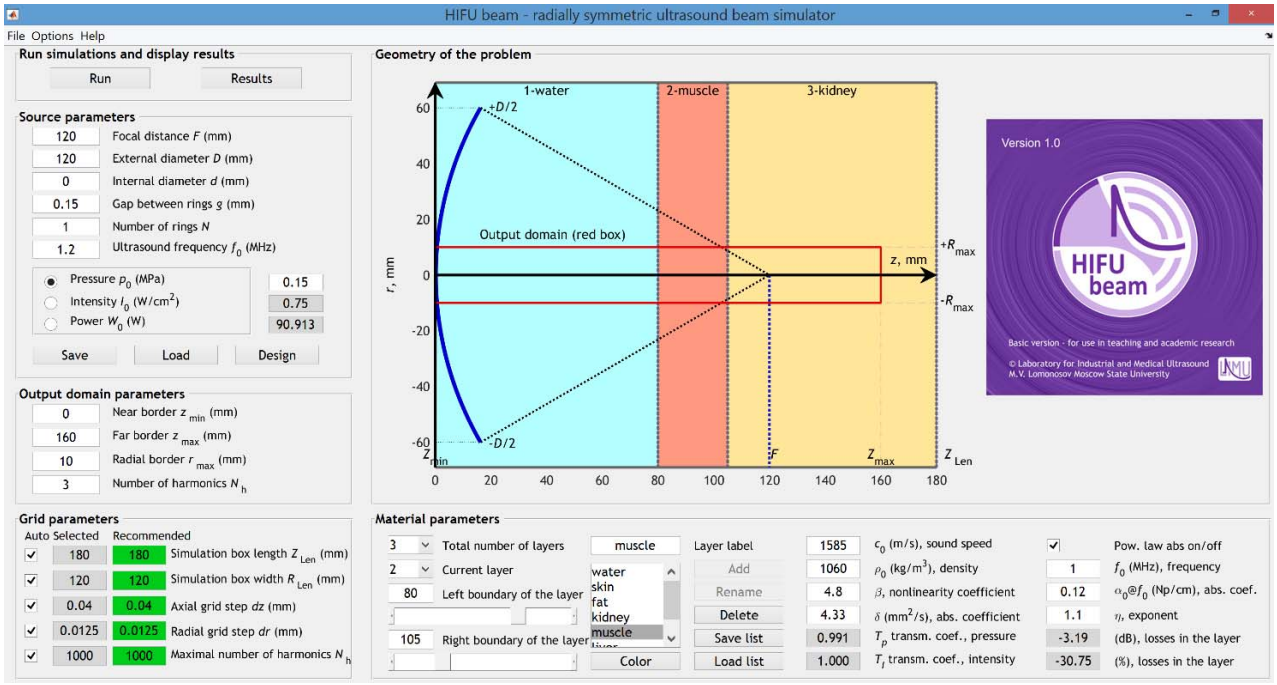

Fig. 1. Software label and main screen of the GUI.

is simulated. The button "Design" displays an additional panel for defining source parameters (in place of the central area). In this design panel, axial electronic focus steering properties, as well as relative amplitude coefficients of individual elements can be specified. The panel also illustrates the prescribed source in multiple views, provides additional information such as linear focusing gain, and displays a button "Eqv. source" that can be activated to calculate the parameters of an equivalent source boundary condition to the KZK equation in place of a previously defined single-element spherically focused source.

Below the source parameters on the main screen, dimensions of the simulation output domain can be modified as well as the number of harmonics to store. Additional controls for the numerical domain used during the simulation are provided in the bottom left corner—namely radial and axial dimensions of the numerical domain, numerical grid steps, and the maximal number of harmonics $N_{\max}$. These parameters can be defined explicitly or chosen automatically to match recommended values displayed in green.

Additional parameters are contained in the "Options" menu where the user can tune fonts of different interface elements and change the number of parallel threads in the hardware setup. Overall configuration can be saved and loaded from the "File" menu. Note that only the most necessary parameters are allowed to be modified via GUI. Additional tuning parameters are available when using the text interface of the software.

IV. HIFU Beam Simulation Examples

In this section, capabilities of the "HIFU beam" solver for nonlinear acoustic field characterization and calculations for heat deposition sources are demonstrated by three representative examples of typical ultrasonic transducers. Simulation results are shown for both KZK and WAPE modes, single-element transducers and annular array sources, propagation in water as well as in a medium with multiple layers.

A. Single-Element Focused Transducer, Propagation in Water

In the first example, an acoustic field was generated by a single-element source in a shape of a spherical bowl. The simulation represented a transducer with a 100-mm diameter, 90-mm focal distance, 1-MHz operational frequency, and water as the propagation medium. Parameters of water were chosen from default GUI settings: $c_0 = 1500$ m/s, $\rho_0 = 1000$ kg/m^3, $\beta = 3.5$, and $\delta = 4.33$ mm^2/s. This typical laboratory ultrasound source has been also considered in our previous papers [60], [62]. Here, the results of simulations performed in the KZK-mode for an equivalent source model are presented to demonstrate critical nonlinear wave effects relevant to shock-forming focusing conditions and compared the results of modeling using the KZK and WAPE modes of the solver.

When the KZK-mode is chosen, the user indicates parameters of the source in the interface, then corresponding parameters of the equivalent source defined in the initial plane $z = 0$ are recalculated inside the software [59]. For the considered single-element transducer, the parameters of the equivalent source are: diameter 114.06 mm, focal distance 98.27 mm, scaling factor of the source pressure amplitude $p_{0\text{eq}}/p_0 = 0.92$.

Shown in Fig. 2(a) are normalized pressure waveforms obtained at the focus using the KZK-mode for different source pressure amplitudes p_0. At very low source pressure amplitude ($p_0 = 0.015$ MPa), linear propagation is observed and only the fundamental frequency is present in the wave spectrum as

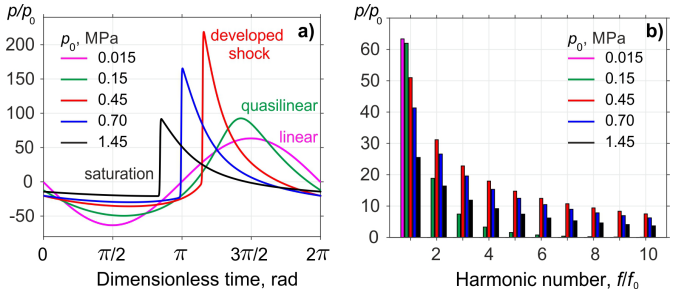

Fig. 2. (a) Focal pressure waveforms and (b) corresponding waveform spectra for various source pressure amplitudes p_0 that reflect different nonlinear regimes of focusing: linear (0.015 MPa), quasi-linear (0.15 MPa), developed shock formation (0.45 MPa), and saturated shocks (0.7 and 1.45 MPa). For better visibility, the waveforms are slightly shifted in phase.

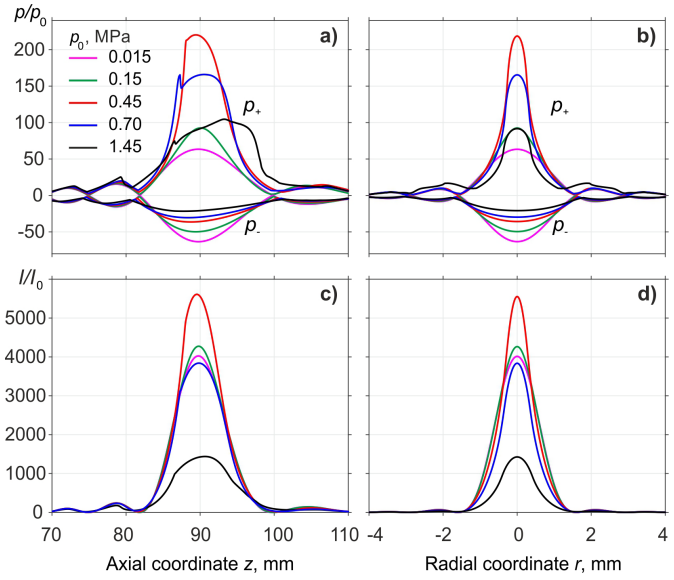

Fig. 3. (a) and (b) Distributions of the normalized peak positive (p_+) and peak negative (p_-) pressures. (c) and (d) Distributions of intensity normalized on its value I_0 on source elements along (a) and (c) axial coordinate and (b) and (d) radial one at the focal plane.

shown in Fig. 2(b). With increasing pressure p_0 at the source, nonlinear effects become noticeable and the pressure waveform at the focus begins to become distorted in an asymmetric manner. Following the criterion that 10% of the total wave intensity is distributed over harmonics of the fundamental frequency, the threshold for quasi-linear waveform distortion corresponds to $p_0 = 0.15$ MPa [Fig. 2(a)] [74]. For this waveform, the pressure amplitude of the second harmonic reaches about a third of the amplitude of the fundamental frequency [Fig. 2(b)].

After increasing p_0 beyond the quasi-linear condition threshold of $p_0 = 0.15$ MPa, the formation of a shock front occurs at a certain source pressure level. First, the shock appears near the positive peak of the waveform. Further increase of p_0 causes the bottom edge of the shock to move toward the zero pressure level. When the shock amplitude normalized to the source pressure p_0 reaches a maximum, the nonlinear distortion level can be described to correspond to the formation of a developed shock [60]. At this level, the bottom edge of the shock front in the focal waveform is located at the zero-pressure level, therefore the shock amplitude is equal to the peak positive pressure of the waveform [60]. In the considered example of a single element transducer, the developed shock forms at $p_0 = 0.45$ MPa [Fig. 2(a)].

With further increase of p_0 beyond the level of the developed shock formation in the focal waveform ($p_0 = 0.45$ MPa), the bottom edge of the shock continues to move down below the zero-pressure level. However, the growth rate of the shock front amplitude slows down (Fig. 2(a), waveforms for 0.7 and 1.45 MPa) because of strong energy absorption at the shocks, which begin to form prefocally. For these saturated shocks, the waveform becomes closer to an asymmetric saw-tooth shape [Fig. 2(b)]. Note that "HIFU beam" default interface allows display of pressure waveforms not only at the focus but also along the axial coordinate z (ON-axis at $r = 0$ mm) and along the transverse coordinate r at the focal plane ($z = F$).

Characteristic changes in the shape of the main focal lobe caused by nonlinear effects are illustrated in Fig. 3, where axial [Fig. 3(a) and (c)] and transverse [Fig. 3(b) and (d)] distributions of the normalized peak positive p_+ and peak negative p_- pressures [Fig. 3(a) and (b)] as well as normalized intensity [Fig. 3(c) and (d)] are presented for

TABLE I

CHARACTERISTIC SOURCE PRESSURE $p_0 = |u_n|\rho_0 c_0$ USED IN NONLINEAR SIMULATIONS OF SINGLE-ELEMENT SOURCE USING THE KZK-MODE; CORRESPONDING PEAK POSITIVE PRESSURE (p_+) AND PEAK NEGATIVE PRESSURE (p_-) FOCAL GAINS IN GEOMETRICAL FOCUS, AXIAL AND RADIAL DIMENSIONS OF THE FOCAL REGION AT −3-DB LEVEL CALCULATED FROM THE GEOMETRICAL FOCUS MAXIMUM

p_0 (MPa)	0.015	0.15	0.45	0.70	1.45
p_+ focusing gain	63.4	92.6	218.7	165.5	91.7
p_- focusing gain	63.4	49.6	35.8	29.7	20.8
p_+ axial (mm)	7.8	6.0	5.1	7.4	11.7
p_+ radial (mm)	1.32	0.95	0.52	0.63	0.72
p_- axial (mm)	7.8	9.2	10.7	11.5	12.5
p_- radial (mm)	1.32	1.58	1.86	1.98	2.10

increasing source pressure amplitudes p_0. For linear focusing conditions ($p_0 = 0.015$ MPa), distributions of the peak positive and peak negative pressures are symmetric with respect to zero [Fig. 3(a) and (b)] and the focal pressure gain is equal to 63.4 (Table I). The combined effect of nonlinearity and diffraction leads to significant asymmetry in distributions at higher output levels. In the quasi-linear focusing case ($p_0 = 0.15$ MPa), the focusing gain for the peak positive pressure is 92.6 and for the peak negative pressure is almost twofold less, 49.6. In the case of developed shock formation at the focus ($p_0 = 0.45$ MPa) the focusing gain for the peak positive pressure is 218.7, which is 3.5 times higher than in the linear case; for the peak negative pressure, the focusing gain of 35.8 is 1.7 times lower than in the linear case. The distributions of p_+ and p_- become strongly asymmetric relative to

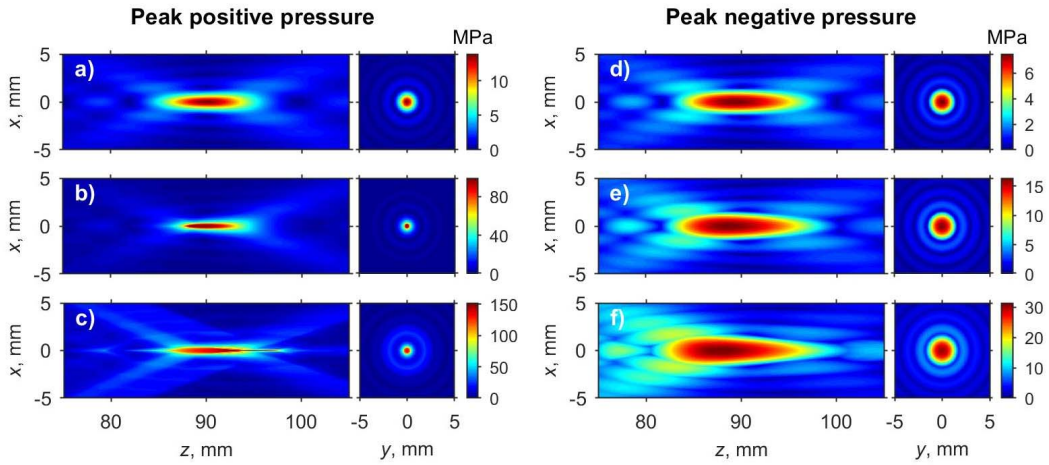

Fig. 4. 2-D spatial distributions of (a)–(c) peak positive pressure and (d)–(f) peak negative pressure in cases of (a) and (d) quasi-linear propagation at $p_0 = 0.15$ MPa, formation of the developed shock at (b) and (e) focus at $p_0 = 0.45$ MPa, and in a saturation regime at $p_0 = 1.45$ MPa.

each other with six times difference in the peak pressure levels. At even higher source pressures, in the saturated focusing conditions the focusing gain for the peak positive pressure is 165.5 and 91.7 for $p_0 = 0.7$ and 1.45 MPa, respectively; corresponding focal gains for the peak negative pressure are 29.7 and 20.8.

Spatial distributions of the intensity change with an increase of the source amplitude following nonlinear changes of the wave spectrum and increased energy deposition when shocks are formed. In the beginning, intensity focusing efficiency increase with the source pressure p_0 due to more efficient focusing of higher harmonics generated in the beam [58], [75]. After the formation of the developed shock, focusing efficiency drops down due to absorption of the wave energy at the shocks that occur prefocally [Fig. 3(c) and (d)]. When increasing p_0 from 0.45 MPa (developed shock) to 1.45 MPa (saturated shock), the focusing gain for the intensity decreased by almost four times [Fig. 3(c) and (d)].

Similar to the focusing gain values, axial and transverse dimensions of the focal area (−3-dB level) for the peak positive pressure change nonmonotonically. Initially, with an increase of the source pressure, axial dimensions of focal areas decrease, reaching their minima when developed shock formation occurs; then, with the formation of saturated shocks, these axial dimensions start to grow slowly. A visual representation of the shape evolution of focal regions of the peak positive and peak negative pressures is provided in Fig. 4. The dimensions of the focal area of the peak positive pressure at −3-dB level start at 7.8 mm × 1.32 mm along the z- and r-coordinates, respectively, in the linear case. These dimensions shrink to 6.0 mm × 0.95 mm in the quasi-linear case [Fig. 4(a)], reach minimum values of 5.1 mm × 0.52 mm in the case of the developed shock formation [Fig. 4(b)], and then grow to 11.7 mm × 0.72 mm in the saturation regime at $p_0 = 1.45$ MPa [Fig. 4(c)]. In the last case, peak positive pressure absolute levels reach about 150 MPa. Note that such a small width of the focal area in the transverse direction r (0.52 mm for $p_0 = 0.45$ MPa) is comparable to the size of a hydrophone tip in experiments and therefore can be affected by an averaging effect and is very sensitive to accurate positioning of the tip. This is the major reason why the peak positive pressures are sometimes underestimated in hydrophone measurements of nonlinear fields at very high source output levels [6]. This averaging effect underlines the benefit and importance of modeling tools when characterizing acoustic fields with fine spatial and temporal structures that develop due to nonlinear propagation effects.

The position of maximum peak positive pressure p_+ changes as the source pressure p_0 increases. In the linear case, the maximum of p_+ is located at $z = 89.8$ mm, slightly closer to the source than the geometrical focus $z = F = 90$ mm. Then, the maximum of the p_+ shifts away from the source to $z = 90.1$ mm even beyond the geometric focus. Furthermore, at $p_0 = 0.45$ MPa it returns closer to the source at $z = 89.5$ mm, and for saturated shocks starts to move away from the source due to a nonlinear defocusing effect ($z = 90.5$ mm and $z = 93.3$ mm for $p_0 = 0.7$ and 1.45 MPa, respectively). The focus shift phenomenon is important to account for in-point hydrophone measurements by indicating at which source output the maximum of p_+ was determined [5], [6].

Unlike the peak positive pressure p_+, the dimensions of the focal area of the peak negative pressure p_- change monotonically with increasing p_0: its dimensions in both directions z and r slightly increase and the focal maximum moves toward the transducer. In the quasi-linear case, the focal area changes from 7.8 mm × 1.32 mm of the linear beam to 9.2 mm × 1.58 mm along the z- and r-coordinates, respectively [Fig. 4(d)]. In the case of the developed shock formation corresponding sizes increase to 10.7 mm × 1.86 mm [Fig. 4(e)] and in the saturation regime become 12.5 mm × 2.1 mm [Fig. 4(f)].

At source pressure levels p_0 that correspond to saturation effects at the focus, a specific double-spike structure on the axial distribution of p_+ have observed when using the KZK simulation model. Indeed, such a structure is clearly seen as

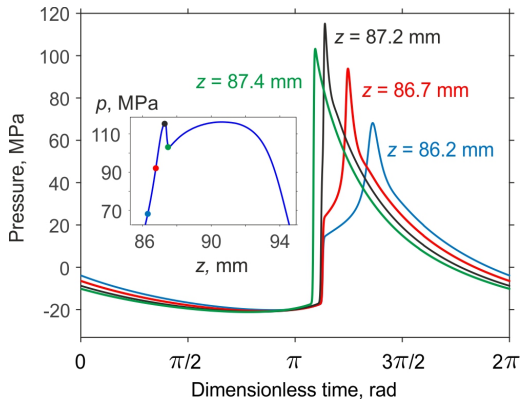

Fig. 5. Axial waveforms at different coordinates z of the focal lobe of p_+ (shown in inset) at $p_0 = 0.7$ MPa. Dots in the inset correspond to coordinates z where waveforms are plotted.

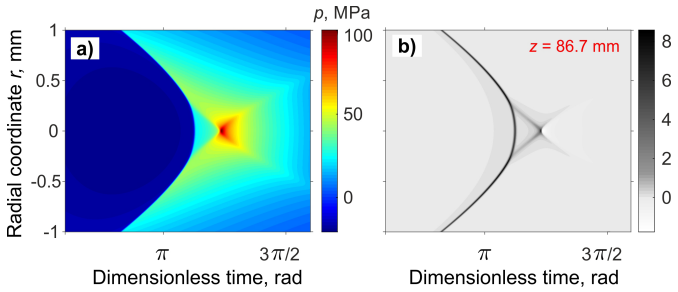

Fig. 6. (a) Temporal pressure waveforms at different transverse distances r from the beam axis and (b) corresponding temporal derivatives of these pressure waveforms ("numerical schlieren image") at fixed prefocal distance $z = 86.7$ mm from the source.

prefocal spikes in Fig. 3(a) on the p_+ curves at $p_0 = 0.7$ MPa and $p_0 = 1.45$ MPa. In order to identify the physical reasons for the formation of such spikes, it is instructive to analyze pressure waveforms in its vicinity (Fig. 5).

A single-element transducer considered here is a piston source that generates direct and edge waves. In the focal lobe of the beam, just before the spike formation near the focus, the pressure waveform contains two fronts (Fig. 5, waveforms at $z = 86.2$ and 86.7 mm). The left (lower) shock in the waveform corresponds to the direct wave while the right (upper) shock comes with the edge wave of the piston source [75]. Since energy absorption at the shock front is proportional to the cube of the shock amplitude $A_{\rm sh}^3$, energy absorption for a wave with two shocks is proportional to the sum of cubes of two shock amplitudes $(A_{\rm sh1}^3 + A_{\rm sh2}^3)$. Propagating closer to the focus, shock fronts of the direct and the edge waves merge at a certain distance (Fig. 5, waveform at $z = 87.2$ mm). Exactly at this distance, the top of the spike is located. After merging of these two shocks, energy absorption is proportional to $(A_{\rm sh1} + A_{\rm sh2})^3$ and increases sharply because of inequality $(A_{\rm sh1} + A_{\rm sh2})^3 > (A_{\rm sh1}^3 + A_{\rm sh2}^3)$ leading to the drop in the amplitude of the resulting merged shock and the peak pressure of the waveform (Fig. 5, the waveform at $z = 87.4$ mm). Since this shock–shock interaction occurs prefocally, a sharp decrease of p_+ returns back to increase due to diffraction amplification near the focus. Similar shock-shock interactions have been observed previously [76], [78].

In aeroacoustics, a similar interaction of shock fronts occurs near a reflecting boundary when the Mach stem forms [79]. It is common to visualize the Mach stem in experiments by using the schlieren technique. Here, a numerical imitation of the schlieren image of the beam is presented in order to show the structure and geometry of the shock fronts. Shown in Fig. 6(a) are pressure waveforms at different transverse distances r from the beam axis at a distance $z = 86.7$ mm from the source. At this distance, the edge and the central waves have not yet merged. 2-D distribution of the temporal derivative of these pressure waveforms [Fig. 6(b)] is an analogy of a schlieren image. The dark stripe on this image corresponds to the location of the shock front in the central wave while the front of the edge waves is represented by brighter gray lines. It is clearly seen that the merging of shocks of the central and edge waves occurs inside the triangle formed at the central part between these fronts [Fig. 6(b)]. After merging, the Mach stem forms perpendicular to the beam axis (not shown here).

The physical mechanism behind the formation and merging of two shocks within one wave period is diffraction, in particular, the arrival of the edge waves. The phenomenon of shock–shock interaction is quite subtle to study since the fine structure of shock fronts should be analyzed for correct description and interpretation. Since the KZK equation takes into account diffraction effects in a parabolic approximation, a logical question here is whether such spatial structures caused by shock–shock interaction are correctly described in the parabolic approximation.

In order to test this, additional simulations were performed in the WAPE-mode of "HIFU beam." For both KZK and WAPE modes, the numerical grids were the same for the same values of p_0 chosen as recommended grid parameters provided in the interface. The radial grid step was 0.0125 mm for all calculations, the maximal harmonic number was 1000, the axial grid step was 0.08 mm for linear propagation, 0.04 mm for quasi-linear and developed shock formation cases, 0.025 mm for $p_0 = 0.7$ MPa, and 0.0125 mm for $p_0 = 1.45$ MPa. The runtime of the simulated examples ranged from 2 min (linear case) to 1 h 17 min (saturated shock at $p_0 = 1.45$ MPa) in the KZK-mode and from 6 min to 2 h 10 min for corresponding cases in the WAPE-mode. Simulations were performed on a desktop PC with AMD Ryzen 3800X 8 physical core processor.

Overall, the results obtained with these two models were in very good agreement within a few percent demonstrating that the combination of the KZK equation with the equivalent source model provides a characterization of the acoustic nonlinear fields with high accuracy. For example, the difference between the peak positive and peak negative pressures at the geometrical focus does not exceed 3%. The greatest discrepancy was observed in the vicinity of the spike, for $p_0 = 0.7$ MPa, where the effect of shock-shock peak formation resulted in peak positive pressure about 8% higher for the KZK model than predicted by the WAPE model (Fig. 7). Our recommendation is to exclude this spike from the evaluation of the maximum values of the peak positive pressure or use

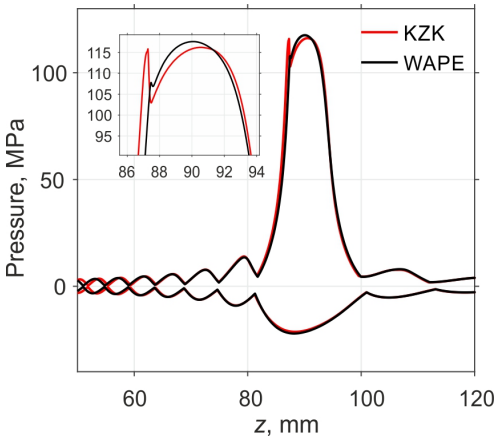

Fig. 7. Axial distributions of the peak positive (p_+) and peak negative (p_-) pressures at $p_0 = 0.7$ MPa obtained using the KZK and WAPE modes of the "HIFU beam" software.

the WAPE-mode of the "HIFU beam" if there is no preference to simulate the KZK equation.

B. Annular Array, Propagation in Water

The next example of a typical HIFU source is an annular array used in the development of thermal and mechanical methods of tissue ablation in mouse tumors [80], [81]. The source is a 16-element annular array (3-MHz frequency, 48-mm diameter, and 35-mm radius of curvature, and 0.15-mm spatial gaps between the elements). In calculations of the acoustic field in water, WAPE-mode was used and specific nonlinear effects related to electronic focus steering are illustrated.

Simulations were performed for linear, quasi-linear, and developed shock formation cases. In the first series of simulations, there was no additional phasing of the array elements. When focusing at the geometrical focus of the array, the quasi-linear case corresponds to $p_0 = 0.14$ MPa and the developed shock forms at the focus at $p_0 = 0.425$ MPa. The case corresponding to saturation was simulated for $p_0 = 0.75$ MPa. In the second series of simulations, the focus was steered to the distance $z = 30$ mm by adding phases to the array elements. In this case, the waveform at the steered focus is quasi-linear at $p_0 = 0.17$ MPa, and the formation of a developed shock at the steered focus occurred at $p_0 = 0.525$ MPa. The saturation case was also simulated for $p_0 = 0.75$ MPa to show the differences arising at the same source output with and without focus steering. Grid steps were chosen the same for both series of simulations: 0.0025 mm in radial direction r and 0.025 mm in the axial direction z, a maximal number of harmonics 1000. Runtimes were from 18 min (linear case) to 2 h (developed shock formation case) on the desktop PC mentioned above.

Pressure waveforms shown in Fig. 8 correspond to three degrees of nonlinear waveform distortion at the focus (quasi-linear, formation of the developed shock, and saturation) when focusing at the geometrical focus [Fig. 8(a)] and steered 5 mm closer to the source [Fig. 8(b)]. Small dimensions of the source and its relatively high operation frequency (3 MHz) allow for generating shock fronts of very high amplitude

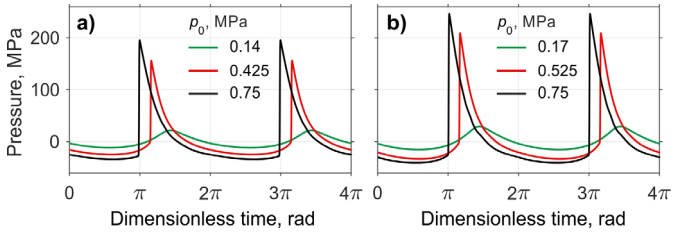

Fig. 8. (a) Pressure waveforms at the focus $z = F = 35$ mm for quasi-linear ($p_0 = 0.14$ MPa), developed shock formation ($p_0 = 0.425$ MPa), and saturation ($p_0 = 0.75$ MPa) cases. (b) Pressure waveforms at steered focus $z = 30$ mm for quasi-linear ($p_0 = 0.17$ MPa), developed shock formation ($p_0 = 0.525$ MPa), and saturation ($p_0 = 0.75$ MPa) cases.

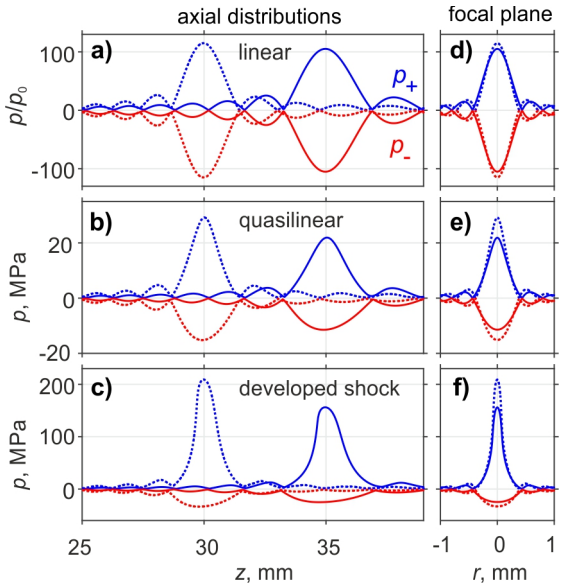

Fig. 9. Peak positive (p_+) and peak negative (p_-) pressure distributions along (a)–(c) z-axis of the annular array and (d)–(f) at the focal plane along the radial coordinate r. (a) and (d) For linear propagation pressure is normalized to the source pressure amplitude p_0. (b) and (e) For quasi-linear and (c) and (f) developed shock formation cases dimensional pressure is plotted. Solid curves: focusing at the geometrical focus $z = 35$ mm. Dotted curves: focusing at the steered focus $z = 30$ mm.

(about 200 MPa) at the focus. Steering the focus toward the source increases the focusing angle which is the most important parameter of the source that controls nonlinear effects, characteristic source output for shock-forming conditions, and characteristic amplitude of the developed shock at the focus [60], [82]. When the focus is steered at $z = 30$ mm, the beam has a higher focusing angle than without steering, the developed shock forms at higher pressure levels ($p_0 = 0.525$ versus 0.425 MPa) and has greater amplitude (Fig. 8).

The sizes of the focal lobe also change with changing of the focusing angle. Weakly focused beams have longer focal lobes as is clearly seen in peak pressure distributions: the focal lobe in the case of steering is narrower in both z- and r-directions than in the case without steering (Fig. 9). Thus, for the considered 16-element array, steering the focus 5 mm closer to the source leads to the following relative characteristics: smaller dimensions of the main focal lobe; formation of a developed shock front of higher amplitude and

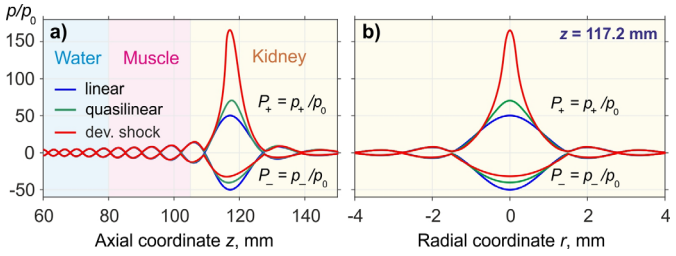

Fig. 10. (a) Axial and (b) radial distributions of normalized peak positive and peak negative pressures for linear, quasi-linear ($p_0 = 0.15$ MPa), and developed shock formation ($p_0 = 0.375$ MPa) cases. Radial distribution (b) is plotted at $z = 117.2$ mm, where a maximum of pressure amplitude in linear propagation locates.

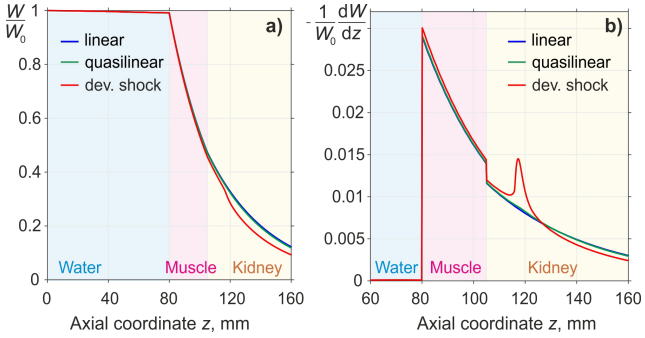

Fig. 11. Distributions of (a) total acoustic beam power W and (b) losses of power dW/dz, both normalized to the initial acoustic power W_0, along the beam axis z for linear, quasi-linear ($p_0 = 0.15$ MPa), and developed shock formation ($p_0 = 0.375$ MPa) cases.

at a higher source pressure; higher pressure levels at the steered focus in the saturation regime of focusing. These effects should be taken into account and can be analyzed using "HIFU beam" when designing annular arrays, characterizing their nonlinear fields, and testing nonlinear steering capabilities when shockwave exposure protocols are developed.

C. Single Element Spherical HIFU Source, Multilayered Medium

The last example is a single-element spherically focused transducer with parameters comparable to those from the 256-element array used in the clinical Sonalleve V1 MRgHIFU system (Profound Medical Corp., Mississauga, ON, Canada) [5]. Specifically, we consider a single-element source with operating frequency $f_0 = 1.2$ MHz, the focal distance $F = 120$ mm, and diameter $D = 120$ mm. Propagation is considered in a layered medium consisting of water ($0 \le z \le 80$ mm), muscle (80 mm $\le z \le 105$ mm), and kidney ($z \ge 105$ mm). Parameters of tissues were selected from default "HIFU beam" tissue profiles [63]: $c_0 = 1585$ m/s, $\rho_0 = 1060$ kg/m^3, $\beta = 4.8$, $\delta = 4.33$ mm^2/s, $\alpha_0 = 0.12$ Np/cm/MHz, $\eta = 1.1$ for muscle and $c_0 = 1570$ m/s, $\rho_0 = 1050$ kg/m^3, $\beta = 4.7$, $\delta = 4.33$ mm^2/s, $\alpha_0 = 0.1$ Np/cm/MHz, $\eta = 1.1$ for kidney. Simulations were performed in the WAPE-mode for linear, quasi-linear ($p_0 = 0.15$ MPa), and developed shock formation ($p_0 = 0.375$ MPa) cases. Grid steps were chosen to be 0.0025 mm in the radial direction r and 0.025 mm in the axial direction z, with 1000 as the maximal number of harmonics. Runtimes were from 16 min (linear case) to 1 h (developed shock formation case) on desktop PC mentioned above.

In the presence of tissue layers, the maxima of the peak positive pressure p_+ and the absolute value of the peak negative pressure $|p_-|$ are reached closer to the source than would occur in water because of refraction effects. For this transducer with focal distance $F = 120$ mm, the maximum linear pressure amplitude in water is located at $z = 119.8$ mm (not shown here). In the water-muscle-kidney medium, the peak is shifted 2.6 mm closer to the source at $z = 117.2$ mm [Fig. 10(a)]. The linear focal gain in water is 80.8 but decreases to about 50 in the absorptive layered medium [Fig. 10(a)].

Similar to the previous examples with propagation only in water, nonlinear beam focusing in tissue layers exhibits an increase in the focusing gain of p_+ until developed shock formation occurs. In the quasi-linear case, the focal gain of p_+ reaches 70 (Fig. 10). When developed shocks form at the focus, the focal gain for p_+ is 165. However, the amplitude of the developed shock is only about 60 MPa because the higher value of the nonlinearity parameter in tissue leads to shock formation at a lower pressure level.

With an increase of p_0 beyond the level of developed shock formation, shocks are present not only at the focus but also in adjacent regions. Moreover, the focusing gain begins to decrease and the size of the focal area increases (not shown here). The focal lobe of the peak negative pressure p_- also behaves in the same way as in previous cases: it grows in the axial direction z as p_0 increases and its maximum moves toward the source (Fig. 10). Thus, the presence of tissue layers does not qualitatively change the manifestation of nonlinear effects close to the focus. However, achieving comparable shocked focal waveforms requires higher source output levels to compensate for absorption effects in tissue as well as the altered shock-forming conditions related to the higher nonlinearity of tissue. These effects are used in methods of nonlinear derating when acoustic field parameters obtained in water are recalculated for propagation in tissue [57], [83].

In addition to characterizing acoustic properties of nonlinear fields, the "HIFU beam" software also allows for evaluating the thermal effect of ultrasound focusing on tissue. Options available to the user are the visualization of a change of the total acoustic beam power W with the propagation distance as well as 1-D and 2-D distributions of the heat deposition rate.

In the linear case, the total acoustic power of a beam in tissue decreases exponentially [Fig. 11(a)]. The formation of the shock front leads to additional heat deposition proportional to the cube of the shock amplitude A_{sh}^3. As shown clearly in Fig. 11(a), in the case of developed shock formation the decrease of the total beam power significantly deviates from the exponential law close to the focus after the "muscle-kidney" boundary. In the focal region, there is a sharp jump in power loss caused by shock formation [Fig. 11(b)]. Despite the fact that normalized total losses of the beam power in the focus differ by only about two times between the linear beam focusing and nonlinear regime with the developed shocks in the focus [Fig. 11(b)], these losses are distributed over

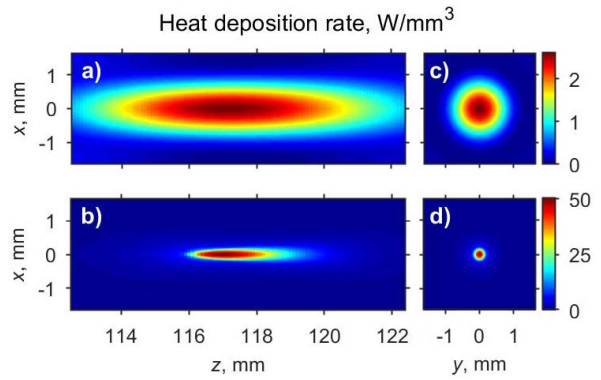

Fig. 12. Heat sources in (a) and (b) axial *zr* and (c) and (d) focal *xy*-planes for the same power of 568 W (a) and (c) when ultrasound propagation model is linear and (b) and (d) nonlinear with developed shock formation at the focus.

different volumes (Fig. 12): axial and radial sizes of focal areas for heat sources are three times smaller when developed shock formation occurs (Fig. 12). This results in a significant difference in the local heat deposition at the focus. In the linear case, calculated for the same power as for developed shock formation (568 W, $p_0 = 0.375$ MPa), the maximum heat deposition rate is 2.6 W/mm^3 while for nonlinear propagation it is about 20 times higher (50.6 W/mm^3).

Thus, shock wave exposure protocols can provide very fast heating of tissue in a very localized volume. This rapid heating has been used in boiling histotripsy methods and in developing methods of fast volumetric thermal tissue ablation by shock waves in existing clinical HIFU systems [61], [83]–[86].

V. Discussion

The "HIFU beam" software presented in this article represents knowledge accumulated over many years for simulating nonlinear focused ultrasound beams using a paradigm of one-way propagation equations. Incorporation of a method of fractional steps with an operator-splitting procedure allowed for applying the most efficient numerical schemes when simulating various physical effects. For example, the diffraction operator is effectively solved in the frequency domain both in parabolic and wide-angle formulations. The wide-angle diffraction equation is commonly used in underwater and atmospheric acoustics [66], [87]; however, only a few papers use this method in the medical ultrasound community, which suggests that its potential is not fully appreciated for such applications. In the radially symmetric case, the wide-angle method is much more efficient than the angular spectrum method based on Hankel functions [45] since the finite-difference scheme produces systems of linear equations with tridiagonal matrices, which are easy to invert. Additionally, PML can be naturally incorporated in the finite-difference schemes allowing more compact numerical domains. It also should be noted that an error of Padé approximations can be regulated depending on a particular problem by changing the approximation order, thereby providing a tradeoff between accuracy and computational speed. As a rule, strongly focused beams require higher approximation orders M than weakly focused beams. The default value $M = 3$ available in the software GUI should be sufficient for most practical cases. The use of a dual-domain solver of the nonlinear operator allows for computational efficiency both for weakly nonlinear fields with a small number of harmonics and for strongly nonlinear cases when the discrete spectrum is fully populated and time-domain methods are more efficient than spectral methods.

Even though "HIFU beam" is limited to axially symmetric fields, it can be used for examining a large number of typical scenarios. Three important cases for its use are noted. One case involves the characterization of ultrasound fields generated in water by existing transducers when the source is axially symmetric [2] or its field can be approximated by the field of an equivalent axially symmetric source [5], [60], [61]. Second, together with guidance from the solution of the inverse nonlinear problem for the field of a focused transducer [82], "HIFU beam" can be used for designing new transducers that generate ultrasound fields with desired nonlinear parameters in the focal region [88]. In addition to providing design assistance for single-element transducers, the "HIFU beam" can also be used to test the nonlinear steering capabilities of annular arrays when developing shockwave exposure protocols [81]. Third, the software is helpful in predicting nonlinear ultrasound fields in biological tissue, which may be useful for protocol design and treatment planning. Although an approximation of a flat-layered propagation medium model is included, the "HIFU beam" could be useful in accounting for absorption over the path length from the source to the focus for making nonlinear derating estimates.

The bright side of the most crucial simplification of the model—axial symmetry—is that the computational burden is moderate. Consequently, the "HIFU beam" can be run on typical desktop or laptop computers. Actual run time will depend on how strong nonlinear effects are and what are the source dimensions. Quasi-linear fields are calculated in several minutes or at least in tens of minutes. Run time for strongly nonlinear fields with shocks can reach several hours. Also, a transducer with a larger diameter will need longer computations than a smaller transducer. To improve performance, a user should correctly set the number of threads for parallel computations and choose executable file specification, which is compliant with the processor architecture. The run time also significantly depends on the values of numerical grid steps. Note that recommended values of the numerical grid steps are given for guidance only and are not mandatory. User responsibilities include the need to check if a particular simulation converges numerically and produces results that reasonably match any available analytic solutions or known data from published papers. In the typical use-cases reported in the paper verification of numerical convergence was performed by the authors.

VI. Conclusion

In this article, a freely available software package (freeware) named "HIFU beam" [1] is described for simulating axially symmetric high-intensity ultrasound beams. The software comprises a solver for models based on the KZK and Westervelt equations as well as GUI tools for defining relevant boundary conditions and physical properties of the simulation domain and visualizing the simulation results. These tools and numerical algorithms of the software are

briefly described. The functionality of the software and specific nonlinear wave phenomena is demonstrated by simulating three typical usage examples: the ultrasound field of a strongly focused single-element transducer in water; the field of an annular array with focus steering in water; and the field of a single-element transducer in layered tissue. The method of an equivalent source applicable for modeling strongly focused single-element transducers using the KZK equation is included. It was shown that the "HIFU beam" allows efficient simulation of focused ultrasound fields in a wide range of intensities including the formation of high-amplitude shock fronts at the focus. Such simulations can help in academic courses, research on designing transducers and characterizing their fields, as well as developing nonlinear exposure protocols for therapeutic applications. In addition, given that current efforts within the international standards community seek to identify and standardize the use of numerical simulations for characterizing therapeutic medical ultrasound fields, "HIFU beam" may have relevant uses for providing calculations against which results from other simulation tools can be compared.

Acknowledgment

The authors are grateful to our colleagues Alex Peek and Ekaterina Ponomarchuk, who have contributed to "HIFU beam" implementation through testing, user feedback, fruitful discussions, and bug reports.

References

[1] (2021). *HIFU Beam*. [Online]. Available: http://limu.msu.ru/node/3555?language=en

[2] M. S. Canney, M. R. Bailey, L. A. Crum, V. A. Khokhlova, and O. A. Sapozhnikov, "Acoustic characterization of high intensity focused ultrasound fields: A combined measurement and modeling approach," *J. Acoust. Soc. Amer.*, vol. 124, no. 4, pp. 2406–2420, Oct. 2008.

[3] J. Wójcik, T. Kujawska, A. Nowicki, and P. A. Lewin, "Fast prediction of pulsed nonlinear acoustic fields from clinically relevant sources using time-averaged wave envelope approach: Comparison of numerical simulations and experimental results," *Ultrasonics*, vol. 48, no. 8, pp. 707–715, Dec. 2008.

[4] O. V. Bessonova and V. Wilkens, "Membrane hydrophone measurement and numerical simulation of HIFU fields up to developed shock regimes," *IEEE Trans. Ultrason., Ferroelectr., Freq. Control*, vol. 60, no. 2, pp. 290–300, Feb. 2013.

[5] W. Kreider *et al.*, "Characterization of a multi-element clinical HIFU system using acoustic holography and nonlinear modeling," *IEEE Trans. Ultrason., Ferroelectr., Freq. Control*, vol. 60, no. 8, pp. 1683–1698, Aug. 2013.

[6] M. M. Karzova *et al.*, "Shock formation and nonlinear saturation effects in the ultrasound field of a diagnostic curvilinear probe," *J. Acoust. Soc. Amer.*, vol. 141, no. 4, pp. 2327–2337, Apr. 2017.

[7] E. Martin, J. Jaros, and B. E. Treeby, "Experimental validation of k-wave: Nonlinear wave propagation in layered, absorbing fluid media," *IEEE Trans. Ultrason., Ferroelectr., Freq. Control*, vol. 67, no. 1, pp. 81–91, Jan. 2020.

[8] P. Gélat, G. ter Haar, and N. Saffari, "A comparison of methods for focusing the field of a HIFU array transducer through human ribs," *Phys. Med. Biol.*, vol. 59, no. 12, pp. 3139–3171, May 2014.

[9] C. Liu and Y. Zhou, "Detection of gaps between high-intensity focused ultrasound (HIFU)-induced lesions using transient axial shear strain elastograms," *Med. Phys.*, vol. 45, no. 8, pp. 3831–3847, Aug. 2018.

[10] P. V. Yuldashev, S. M. Shmeleva, S. A. Ilyin, O. A. Sapozhnikov, L. R. Gavrilov, and V. A. Khokhlova, "The role of acoustic nonlinearity in tissue heating behind a rib cage using a high-intensity focused ultrasound phased array," *Phys. Med. Biol.*, vol. 58, no. 8, pp. 2537–2559, Apr. 2013.

[11] V. Suomi, J. Jaros, B. Treeby, and R. Cleveland, "Nonlinear 3-D simulation of high-intensity focused ultrasound therapy in the kidney," in *Proc. 38th Annu. Int. Conf. IEEE Eng. Med. Biol. Soc. (EMBC)*, Aug. 2016, pp. 5648–5651.

[12] N. Albin, O. P. Bruno, T. Y. Cheung, and R. O. Cleveland, "Fourier continuation methods for high-fidelity simulation of nonlinear acoustic beams," *J. Acoust. Soc. Amer.*, vol. 132, no. 4, pp. 2371–2387, Oct. 2012.

[13] U. Vyas and D. Christensen, "Ultrasound beam simulations in inhomogeneous tissue geometries using the hybrid angular spectrum method," *IEEE Trans. Ultrason., Ferroelectr., Freq. Control*, vol. 59, no. 6, pp. 1093–1100, Jun. 2012.

[14] J. L. B. Robertson, B. T. Cox, J. Jaros, and B. E. Treeby, "Accurate simulation of transcranial ultrasound propagation for ultrasonic neuromodulation and stimulation," *J. Acoust. Soc. Amer.*, vol. 141, no. 3, pp. 1726–1738, Mar. 2017.

[15] P. B. Rosnitskiy, P. V. Yuldashev, O. A. Sapozhnikov, L. R. Gavrilov, and V. A. Khokhlova, "Simulation of nonlinear trans-skull focusing and formation of shocks in brain using a fully populated ultrasound array with aberration correction," *J. Acoust. Soc. Amer.*, vol. 146, no. 3, pp. 1786–1798, Sep. 2019.

[16] J. Gu and Y. Jing, "A modified mixed domain method for modeling acoustic wave propagation in strongly heterogeneous media," *J. Acoust. Soc. Amer.*, vol. 147, no. 6, pp. 4055–4068, Jun. 2020.

[17] *Ultrasonics–Field Characterization–Specification and Measurement of Field Parameters for High Intensity Therapeutic Ultrasound (HITU) Transducers and Systems*, Standard IEC/TS 62556 Ed., International Electrotechnical Commission, Geneva, Switzerland, 1.0, 2014.

[18] U.S. Food and Drug Administration / Center for Devices and Radiological Health. (2016). *Reporting of Computational Modeling Studies in Medical Device Submissions–Guidance for Industry and Food and Drug Administration Staff*. [Online]. Available: https://www.fda.gov/regulatory-information/search-fda-guidance-documents/reporting-computational-modeling-studies-medical-device-submissions

[19] M. D. Verweij, B. E. Treeby, K. W. A. van Dongen, and L. Demi, "Simulation of ultrasound fields," in *Comprehensive Biomedical Physics*, vol. 2. Oxford, U.K.: Elsevier, 2014, ch. 2.19, pp. 465–499.

[20] J. Gu and Y. Jing, "Modeling of wave propagation for medical ultrasound: A review," *IEEE Trans. Ultrason., Ferroelectr., Freq. Control*, vol. 62, no. 11, pp. 1979–1993, Nov. 2015.

[21] J. Berntsen, "Numerical calculations of finite amplitude sound beams," in *Frontiers of Nonlinear Acoustics*. New York, NY, USA: Springer, 1990, pp. 191–196.

[22] Y.-S. Lee and M. F. Hamilton, "Time-domain modeling of pulsed finite-amplitude sound beams," *J. Acoust. Soc. Amer.*, vol. 97, no. 2, pp. 906–917, Feb. 1995.

[23] R. J. McGough, "Rapid calculations of time-harmonic nearfield pressures produced by rectangular pistons," *J. Acoust. Soc. Amer.*, vol. 115, no. 5, pp. 1934–1941, May 2004.

[24] M. E. Frijlink, H. Kaupang, T. Varslot, and S.-E. Masoy, "Abersim: A simulation program for 3D nonlinear acoustic wave propagation for arbitrary pulses and arbitrary transducer geometries," in *Proc. IEEE Ultrason. Symp.*, Nov. 2008, pp. 1282–1285.

[25] J. E. Soneson, "A user-friendly software package for HIFU simulation," in *Proc. AIP Conf.*, 2009, vol. 1113, no. 1, pp. 165–169.

[26] B. E. Treeby and B. T. Cox, "*K*-wave: MATLAB toolbox for the simulation and reconstruction of photoacoustic wave fields," *J. Biomed. Opt.*, vol. 15, no. 2, p. 021314-12, Mar. 2010.

[27] F. Varray, A. Ramalli, C. Cachard, P. Tortoli, and O. Basset, "Fundamental and second-harmonic ultrasound field computation of inhomogeneous nonlinear medium with a generalized angular spectrum method," *IEEE Trans. Ultrason., Ferroelectr., Freq. Control*, vol. 58, no. 7, pp. 1366–1376, Jul. 2011.

[28] J. A. Jensen, "A multi-threaded version of field II," in *Proc. IEEE Int. Ultrason. Symp.*, Sep. 2014, pp. 2229–2232.

[29] D. Yevick and D. J. Thomson, "Complex Padé approximants for wide-angle acoustic propagators," *J. Acoust. Soc. Amer.*, vol. 108, no. 6, pp. 2784–2790, Dec. 2000.

[30] D. Yevick and D. J. Thomson, "Impedance-matched absorbers for finite-difference parabolic equation algorithms," *J. Acoust. Soc. Amer.*, vol. 107, no. 3, pp. 1226–1234, Mar. 2000.

[31] A. Kurganov and E. Tadmor, "New high-resolution central schemes for nonlinear conservation laws and convection–diffusion equations," *J. Comput. Phys.*, vol. 160, no. 1, pp. 241–282, May 2000.

[32] R. J. Zemp, J. Tavakkoli, and R. S. C. Cobbold, "Modeling of nonlinear ultrasound propagation in tissue from array transducers," *J. Acoust. Soc. Amer.*, vol. 113, no. 1, pp. 139–152, Jan. 2003.

[33] T. Kamakura, H. Nomura, and G. Clement, "Application of the split-step Padé approach to nonlinear field predictions," *Ultrasonics*, vol. 53, no. 2, pp. 432–438, Feb. 2013.

[34] G. Pinton, J. Dahl, S. Rosenzweig, and G. Trahey, "A heterogeneous nonlinear attenuating full- wave model of ultrasound," *IEEE Trans. Ultrason., Ferroelectr., Freq. Control*, vol. 56, no. 3, pp. 474–488, Mar. 2009.

[35] M. Solovchuk, T. W. H. Sheu, and M. Thiriet, "Simulation of nonlinear westervelt equation for the investigation of acoustic streaming and nonlinear propagation effects," *J. Acoust. Soc. Amer.*, vol. 134, no. 5, pp. 3931–3942, Nov. 2013.

[36] R. Velasco-Segura and P. L. Rendón, "A finite volume approach for the simulation of nonlinear dissipative acoustic wave propagation," *Wave Motion*, vol. 58, pp. 180–195, Nov. 2015.

[37] B. E. Treeby and B. T. Cox, "Modeling power law absorption and dispersion in viscoelastic solids using a split-field and the fractional Laplacian," *J. Acoust. Soc. Amer.*, vol. 136, no. 4, pp. 1499–1510, Oct. 2014.

[38] J. Jaros, A. P. Rendell, and B. E. Treeby, "Full-wave nonlinear ultrasound simulation on distributed clusters with applications in high-intensity focused ultrasound," *Int. J. High Perform. Comput. Appl.*, vol. 30, no. 2, pp. 137–155, Apr. 2015.

[39] V. A. Khokhlova, A. E. Ponomarev, M. A. Averkiou, and L. A. Crum, "Nonlinear pulsed ultrasound beams radiated by rectangular focused diagnostic transducers," *Acoust. Phys.*, vol. 52, no. 4, pp. 481–489, Jul. 2006.

[40] Y. Jing and R. O. Cleveland, "Modeling the propagation of nonlinear three-dimensional acoustic beams in inhomogeneous media," *J. Acoust. Soc. Amer.*, vol. 122, no. 3, pp. 1352–1364, Sep. 2007.

[41] P. T. Christopher and K. J. Parker, "New approaches to nonlinear diffractive field propagation," *J. Acoust. Soc. Amer.*, vol. 90, no. 1, pp. 488–499, Jul. 1991.

[42] J. Wójcik, A. Nowicki, P. A. Lewin, P. E. Bloomfield, T. Kujawska, and L. Filipczyński, "Wave envelopes method for description of nonlinear acoustic wave propagation," *Ultrasonics*, vol. 44, no. 3, pp. 310–329, Jul. 2006.

[43] Y. Jing, M. Tao, and G. T. Clement, "Evaluation of a wave-vector-frequency-domain method for nonlinear wave propagation," *J. Acoust. Soc. Amer.*, vol. 129, no. 1, pp. 32–46, Jan. 2011.

[44] P. V. Yuldashev and V. A. Khokhlova, "Simulation of three-dimensional nonlinear fields of ultrasound therapeutic arrays," *Acoust. Phys.*, vol. 57, no. 3, pp. 334–343, May 2011.

[45] P. T. Christopher and K. J. Parker, "New approaches to the linear propagation of acoustic fields," *J. Acoust. Soc. Amer.*, vol. 90, no. 1, pp. 507–521, Jul. 1991.

[46] T. Varslot and G. Taraldsen, "Computer simulation of forward wave propagation in soft tissue," *IEEE Trans. Ultrason., Ferroelectr., Freq. Control*, vol. 52, no. 9, pp. 1473–1482, Sep. 2005.

[47] X. Zeng and R. J. McGough, "Evaluation of the angular spectrum approach for simulations of near-field pressures," *J. Acoust. Soc. Amer.*, vol. 123, no. 1, pp. 68–76, Jan. 2008.

[48] X. Zhao, M. F. Hamilton, and R. J. McGough, "Simulations of nonlinear continuous wave pressure fields in FOCUS," in *Proc. 14th Int. Symp. Therapeutic Ultrasound, AIP Conf.*, Mar. 2017, vol. 1821, no. 1, Art. no. 080001.

[49] F. Varray, O. Basset, P. Tortoli, and C. Cachard, "CREANUIS: A nonlinear radiofrequency ultrasound image simulator," *Ultrasound Med. Biol.*, vol. 39, no. 10, pp. 1915–1924, Oct. 2013.

[50] S. I. Aanonsen, T. Barkve, J. N. Tjotta, and S. Tjotta, "Distortion and harmonic generation in the nearfield of a finite amplitude sound beam," *J. Acoust. Soc. Amer.*, vol. 75, no. 3, pp. 749–768, Mar. 1984.

[51] J. E. Soneson, "Extending the utility of the parabolic approximation in medical ultrasound using wide-angle diffraction modeling," *IEEE Trans. Ultrason., Ferroelectr., Freq. Control*, vol. 64, no. 4, pp. 679–687, Apr. 2017.

[52] S. Pozzi, C. Borrazzo, M. Carnì, E. D. Castro, S. Valentini, and B. Caccia, "A computational tool for evaluating HIFU safety," *Ann. Ist. Super. Sanita*, vol. 52, no. 2, pp. 256–260, Jun. 2016.

[53] S. Kashcheeva, O. Sapozhnikov, V. Khokhlova, M. Averkiou, and L. Crum, "Nonlinear distortion and attenuation of intense acoustic waves in lossy media obeying a frequency power law," *Acoust. Phys.*, vol. 46, pp. 170–177, Mar. 2000.

[54] E. A. Filonenko and V. A. Khokhlova, "Effect of acoustic nonlinearity on heating of biological tissue by high-intensity focused ultrasound," *Acoust. Phys.*, vol. 47, no. 4, pp. 468–475, Jul. 2001.

[55] M. V. Aver'yanov, V. A. Khokhlova, O. A. Sapozhnikov, P. Blanc-Benon, and R. O. Cleveland, "Parabolic equation for nonlinear acoustic wave propagation in inhomogeneous moving media," *Acoust. Phys.*, vol. 52, no. 6, pp. 623–632, Dec. 2006.

[56] O. V. Bessonova and V. A. Khokhlova, "Spatial structure of high intensity focused ultrasound beams of various geometry," *Phys. Wave Phenomena*, vol. 17, no. 1, pp. 45–49, Feb. 2009.

[57] O. V. Bessonova, V. A. Khokhlova, M. S. Canney, M. R. Bailey, and L. A. Crum, "A derating method for therapeutic applications of high intensity focused ultrasound," *Acoust. Phys.*, vol. 56, no. 3, pp. 354–363, May 2010.

[58] O. V. Bessonova, V. A. Khokhlova, M. R. Bailey, M. S. Canney, and L. A. Crum, "Focusing of high power ultrasound beams and limiting values of shock wave parameters," *Acoust. Phys.*, vol. 55, nos. 4–5, pp. 463–476, Jul. 2009.

[59] P. B. Rosnitskiy, P. V. Yuldashev, B. A. Vysokanov, and V. A. Khokhlova, "Setting boundary conditions on the Khokhlov–Zabolotskaya equation for modeling ultrasound fields generated by strongly focused transducers," *Acoust. Phys.*, vol. 62, no. 2, pp. 151–159, Apr. 2016.

[60] P. B. Rosnitskiy *et al.*, "Design of HIFU transducers for generating specified nonlinear ultrasound fields," *IEEE Trans. Ultrason., Ferroelectr., Freq. Control*, vol. 64, no. 2, pp. 374–390, Feb. 2017.

[61] A. D. Maxwell *et al.*, "A prototype therapy system for transcutaneous application of boiling histotripsy," *IEEE Trans. Ultrason., Ferroelectr., Freq. Control*, vol. 64, no. 10, pp. 1542–1557, Oct. 2017.

[62] P. V. Yuldashev, I. S. Mezdrokhin, and V. A. Khokhlova, "Wide-angle parabolic approximation for modeling high-intensity fields from strongly focused ultrasound transducers," *Acoust. Phys.*, vol. 64, no. 3, pp. 309–319, Jun. 2018.

[63] F. A. Duck, "Acoustic Properties of Tissue at Ultrasound Frequencies," in *Physical Properties of Tissue*. London, U.K.: Academic, 1990, ch. 4, sec. 4.2, pp. 96–99.

[64] K. R. Waters, J. Mobley, and J. G. Miller, "Causality-imposed (Kramers-Kronig) relationships between attenuation and dispersion," *IEEE Trans. Ultrason., Ferroelectr., Freq. Control*, vol. 52, no. 5, pp. 822–823, May 2005.

[65] W. H. Press, S. A. Teukolsky, W. T. Vetterling, and B. P. Flannery, "Tridiagonal and band diagonal systems of equations," in *Numerical Recipes in FORTRAN. The Art of Scientific Computing*. 2nd ed. Cambridge, U.K.: Cambridge Univ. Press, 1992, ch. 2, sec. 2.4, pp. 42–47.

[66] D. Lee, A. D. Pierce, and E.-C. Shang, "Parabolic equation development in the twentieth century," *J. Comput. Acoust.*, vol. 08, no. 04, pp. 527–637, Dec. 2000.

[67] M. D. Collins, R. J. Cederberg, D. B. King, and S. A. Chin-Bing, "Comparison of algorithms for solving parabolic wave equations," *J. Acoust. Soc. Amer.*, vol. 100, no. 1, pp. 178–182, Jul. 1996.

[68] M. Collins, "A split-step Padé solution for the parabolic equation method," *J. Acoust. Soc. Amer.*, vol. 93, no. 4, pp. 1736–1742, Apr. 1993.

[69] N. Tjotta and S. Tjotta, "Effects of focusing on the nonlinear interaction between two collinear finite amplitude sound beams," *J. Acoust. Soc. Amer.*, vol. 89, no. 3, pp. 1017–1027, Mar. 1991.

[70] G. F. Pinton and G. E. Trahey, "A comparison of time-domain solutions for the full-wave equation and the parabolic wave equation for a diagnostic ultrasound transducer," *IEEE Trans. Ultrason., Ferroelectr., Freq. Control*, vol. 55, no. 3, pp. 730–733, Mar. 2008.

[71] H. T. O'Neil, "Theory of focusing radiators," *J. Acoust. Soc. Amer.*, vol. 21, no. 5, pp. 516–526, Sep. 1949.

[72] O. A. Sapozhnikov, S. A. Tsysar, V. A. Khokhlova, and W. Kreider, "Acoustic holography as a metrological tool for characterizing medical ultrasound sources and fields," *J. Acoust. Soc. Amer.*, vol. 138, no. 3, pp. 1515–1532, Sep. 2015.

[73] A. D. Pierce, "The wave theory of sound," in *Acoustics: An Introduction to its Physical Principles and Applications*, 3rd ed. New York, NY, USA: Springer, 2019, ch. 1, sec. 1.11, pp. 39–42.

[74] *Ultrasonics–Field Characterization*–In Situ *Exposure Estimation in Finite-Amplitude Ultrasonic Beams*, document IEC/TS 61949, 2007.

[75] M. M. Karzova, M. V. Averiyanov, O. A. Sapozhnikov, and V. A. Khokhlova, "Mechanisms for saturation of nonlinear pulsed and periodic signals in focused acoustic beams," *Acoust. Phys.*, vol. 58, no. 1, pp. 81–87, Jan. 2012.

[76] V. A. Khokhlova, R. Souchon, J. Tavakkoli, O. A. Sapozhnikov, and D. Cathignol, "Numerical modeling of finite-amplitude sound beams: Shock formation in the near field of a cw plane piston source," *J. Acoust. Soc. Amer.*, vol. 110, no. 1, pp. 95–108, Jul. 2001.

[77] O. A. Sapozhnikov, V. A. Khokhlova, and D. Cathignol, "Nonlinear waveform distortion and shock formation in the near field of a continuous wave piston source," *J. Acoust. Soc. Amer.*, vol. 115, no. 5, pp. 1982–1987, May 2004.

[78] B. Sturtevant and V. A. Kulkarny, "Thee focusing of weak shock waves," *J. Fluid Mech.*, vol. 73, no. 4, pp. 651–671, Feb. 1976.

[79] M. M. Karzova, V. A. Khokhlova, E. Salze, S. Ollivier, and P. Blanc-Benon, "Mach stem formation in reflection and focusing of weak shock acoustic pulses," *J. Acoust. Soc. Amer.*, vol. 137, no. 6, pp. EL436–EL442, Jun. 2015.

[80] M. Hoogenboom *et al.*, "Development of a high-field MR-guided HIFU setup for thermal and mechanical ablation methods in small animals," *J. Therapeutic Ultrasound*, vol. 3, no. 1, p. 14, Dec. 2015.
[81] V. A. Khokhlova *et al.*, "Reconstruction of nonlinear ultrasound field of an annular therapeutic array from acoustic holograms of its individual elements," *Proc. Meetings Acoust.*, vol. 32, no. 1, Dec. 2017, Art. no. 020013.
[82] P. B. Rosnitskiy, P. V. Yuldashev, and V. A. Khokhlova, "Effect of the angular aperture of medical ultrasound transducers on the parameters of nonlinear ultrasound field with shocks at the focus," *Acoust. Phys.*, vol. 61, no. 3, pp. 301–307, May 2015.
[83] T. D. Khokhlova, M. S. Canney, V. A. Khokhlova, O. A. Sapozhnikov, L. A. Crum, and M. R. Bailey, "Controlled tissue emulsification produced by high intensity focused ultrasound shock waves and millisecond boiling," *J. Acoust. Soc. Amer.*, vol. 130, no. 5, pp. 3498–3510, Nov. 2011, doi: 10.1121/1.3626152.
[84] M. S. Canney, V. A. Khokhlova, O. V. Bessonova, M. R. Bailey, and L. A. Crum, "Shock-induced heating and millisecond boiling in gels and tissue due to high intensity focused ultrasound," *Ultrasound Med. Biol.*, vol. 36, no. 2, pp. 250–267, Feb. 2010.
[85] S. Yu Andriyakhina, M. M. Karzova, P. V. Yuldashev, and V. A. Khokhlova, "Accelerated thermal ablation of biological tissue volumes using HIFU beams with shock fronts," *Acoust. Phys.*, vol. 65, no. 2, pp. 141–150, May 2019.
[86] P. Ramaekers, M. De Greef, J. M. M. Van Breugel, C. T. W. Moonen, and M. Ries, "Increasing the HIFU ablation rate through an MRI-guided sonication strategy using shock waves: Feasibility in the *in vivo* porcine liver," *Phys. Med. Biol.*, vol. 61, no. 3, pp. 1057–1077, Jan. 2016.
[87] V. E. Ostashev, D. K. Wilson, and M. B. Muhlestein, "Wave and extra-wide-angle parabolic equations for sound propagation in a moving atmosphere," *J. Acoust. Soc. Amer.*, vol. 147, no. 6, pp. 3969–3984, Jun. 2020.
[88] V. A. Khokhlova *et al.*, "Design of HIFU transducers to generate specific nonlinear ultrasound fields," *Phys. Procedia*, vol. 87, pp. 132–138, 2016.

Petr V. Yuldashev received the M.S. degree in physics from Moscow State University (MSU), Moscow, Russia, in 2008, and the Ph.D. degree in acoustics from the École Centrale de Lyon (ECL), Ecully, France, in 2011, according to the double Ph.D. program of the French Government.

After graduation from the Ph.D. program, he was appointed by Moscow State University and is currently an Associate Professor at the Department of General Physics and Condensed Matter Physics, Physics Faculty, MSU. He has been affiliated with the Department of Fluid Mechanics, Acoustics, and Energetics, ECL, to work on the propagation of shock waves in a turbulent atmosphere and the utilization of nonlinear acoustics effects to calibrate high-frequency broadband microphones. His research interests pertain to simulation of nonlinear wave propagation in inhomogeneous media, shock wave focusing, sonic booms, and optical measurement methods for acoustic phenomena.

Maria M. Karzova received the M.S. degree in physics from Moscow State University (MSU), Moscow, Russia, in 2012, and the Ph.D. degree in acoustics from the École Centrale de Lyon (ECL), Ecully, France, in 2016, according to the double Ph.D. program of the French Government.

After graduation from the Ph.D. program, she was appointed by Moscow State University, where she is currently a Senior Researcher at the Department of General Physics and Condensed Matter Physics, Physics Faculty. She has been affiliated with the Department of Fluid Mechanics, Acoustics, and Energetics, ECL, to work on irregular reflection of N-waves from smooth and rough surfaces. Her research interests are in nonlinear acoustics, therapeutic ultrasound, and optical methods for measuring acoustical pressure waveforms in air.

Wayne Kreider received the B.S. and M.S. degrees in engineering mechanics at Virginia Tech, Blacksburg, VA, USA, in 1993 and 1995, respectively, and the Ph.D. degree in bioengineering from the University of Washington, Seattle, WA, USA, in 2008.

He is a licensed Professional Engineer with the Commonwealth of Virginia, Richmond, VA, USA. He was an Engineer with the Naval Surface Warfare Center, Dahlgren, VA, USA, and Dominion Engineering Inc., Reston, VA, USA. Since 2001, he has been with the Applied Physics Laboratory (APL), Center for Industrial and Medical Ultrasound, University of Washington. His research interests include acoustic cavitation, transport processes in oscillating bubbles, therapeutic ultrasound, and ultrasound metrology.

Pavel B. Rosnitskiy received the M.S. degree in physics and Ph.D. degree in acoustics from Moscow State University (MSU), Moscow, Russia, in 2016 and 2019, respectively.

He is currently a Junior Research Scientist with the Department of Medical Physics, Physics Faculty, MSU. He was also recognized for the Best Undergraduate Student Project in 2013, the Best M.S. Thesis in 2016, and as the Best Student of the Physics Faculty, MSU, in 2015. His research interests include nonlinear acoustics, ultrasound imaging, design of multielement arrays, and therapeutic applications of high-intensity focused ultrasound waves with shocks.

Dr. Rosnitskiy was awarded by scholarships named after R. V. Khokhlov and S. I. Vavilov, by the Scholarship of the President of Russia from 2014 to 2016, and by the International Student Award from the Acoustical Society of America in 2016 during his studies at MSU.

Oleg A. Sapozhnikov received the M.S. degree in physics and the Ph.D. and D.Sc. degrees in acoustics from Moscow State University (MSU), Moscow, Russia, in 1985, 1988, and 2008, respectively.

He is currently a Professor with the Department of Acoustics, Physics Faculty, MSU. Since 1996, he has been with the Applied Physics Laboratory, Center for Industrial and Medical Ultrasound, University of Washington, Seattle, WA, USA. His research interests are physical acoustics, nonlinear wave phenomena, medical ultrasound, including shock wave lithotripsy, high-intensity focused ultrasound, and ultrasound-based imaging.

Dr. Sapozhnikov has been a member of the Board of International Congress on Ultrasonics since 2009 and the Head of the Physical Ultrasound Division of the Scientific Council on Acoustics of the Russian Academy of Sciences since 2009.

Vera A. Khokhlova received the M.S. degree in physics and the Ph.D. and D.Sc. degrees in acoustics from Moscow State University (MSU), Moscow, Russia, in 1986, 1991, and 2012, respectively.

After graduation from the Ph.D. program, she was appointed by Moscow State University and is currently an Associate Professor at the Department of Acoustics, Physics Faculty, MSU. Since 1995, she has also been with the Center for Industrial and Medical Ultrasound, Applied Physics Laboratory (APL), University of Washington, Seattle, WA, USA. Her research interests are in the field of nonlinear acoustics, therapeutic ultrasound, including metrology and bioeffects of high-intensity focused ultrasound fields, shock wave focusing, nonlinear wave propagation in inhomogeneous media, and nonlinear modeling.